# Objective Categorization of Heavy-Rain-Producing MCS Synoptic Types by Rotated Principal Component Analysis

JOHN M. PETERS AND RUSS S. SCHUMACHER

*Department of Atmospheric Science, Colorado State University, Fort Collins, Colorado*

(Manuscript received 18 September 2013, in final form 8 January 2014)

ABSTRACT

In this research, rotated principal component analysis was applied to the atmospheric fields associated with a large sample of heavy-rain-producing mesoscale convective systems (MCSs). Cluster analysis in the subspace defined by the leading two resulting principal components revealed two subtypes with distinct synoptic and mesoscale characteristics, which are referred to as warm-season-type and synoptic-type events, respectively. Subsequent composite analysis showed that both subtypes typically occurred on the cool side of a quasi-stationary, low-level frontal boundary, within a region of locally maximized low-level convergence and warm advection. Synoptic-type events, which tended to exhibit greater horizontal extent than warm-season-type events, typically occurred downstream of a progressive upper-level trough, along a low-level potential temperature gradient with the warmest air to the south and southeast. Warm-season-type events, on the other hand, occurred within the right-entrance region of a minimally to anticyclonically curved upper-level jet streak, along a low-level potential temperature gradient with the warmest low-level air to the southwest. Synoptic-scale forcing for ascent was stronger in synoptic-type events, while low-level moisture was greater in warm-season-type events. Warm-season-type events were frequently preceded by the passage of a trailing-stratiform- (TS) type MCS, whereas synoptic-type events often occurred prior to the passage of a TS-type system. Analysis of the composite vertical wind profiles at the event location suggests that quasi-stationary behavior in warm-season events predominantly resulted from upstream propagation that nearly canceled advection by the mean steering flow, whereas in the case of synoptic-type events training predominantly resulted from system motion that paralleled a front.

## 1. Introduction

Previous studies of extreme rainfall events in the central and eastern United States [e.g., events that produced reported flash floods (Maddox et al. 1979); events that produced 24-h precipitation greater than the 50-yr recurrence interval for a given location (Schumacher and Johnson 2005, 2006)] have shown that a large percentage of them result from mesoscale convective systems (MCSs, on the order of 60%–75%). Specifically, MCSs tend to produce extreme rainfall when convective rainfall regions are nearly stationary (backbuilding archetype, BB; Fig. 1b), or where motion of a linear convective feature is predominantly line parallel (training-line/adjoining-stratiform archetype, TL/AS; Fig. 1a), resulting in persistence of convective cells over a particular geographic region (Schumacher and Johnson 2005, 2006). Composite analysis of such events shows that they tend to thrive within an elevated conditionally unstable layer along the northern periphery of a southerly low-level jet, within a region of persistent isentropic upglide and associated large-scale layer lifting (Maddox et al. 1979; Moore et al. 2003; Schumacher and Johnson 2005; Schumacher and Johnson 2008). Since the aforementioned synoptic-scale environment is also conducive to progressive MCSs [which less commonly produce excessive rainfall amounts; e.g., Parker and Johnson (2000); Laing and Fritsch (2000)], and sometimes progressive and quasi-stationary MCSs adjacent to one another [e.g., Corfidi (2003); the bow and arrow phenomena described by Keene and Schumacher (2013)], it is of particular meteorological importance to understand the specific meso-$\alpha$- to synoptic-scale factors that are conducive to slow-moving MCSs (as well as the variability therein).

Most composite analyses in previous studies of MCS archetypes have utilized groupings of cases selected

*Corresponding author address:* John M. Peters, Dept. of Atmospheric Science, Colorado State University, 1371 Campus Delivery, Fort Collins, CO 80521.
E-mail: jpeters3@atmos.colostate.edu

DOI: 10.1175/MWR-D-13-00295.1

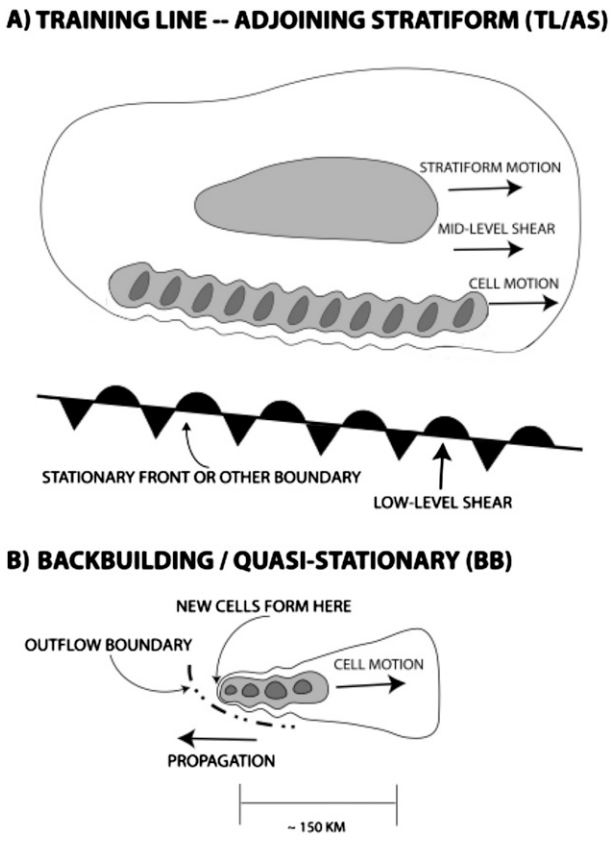


FIG. 1. Schematic of the salient radar reflectivity features associated with the two predominant heavy-rain-producing MCS archetypes: (a) TL/AS and (b) BB. [From Schumacher and Johnson (2005).]

based on their subjectively identified radar reflectivity characteristics. While a grouping of MCSs may exhibit similar radar morphologies, there is no guarantee that they occur within similar synoptic-scale environments. For instance, previous authors have differentiated "synoptic type" heavy rainfall, which often involves the passage of multiple distinct MCSs and where convection persists over a fixed geographic region for over 24 h (Maddox et al. 1979; Schumacher and Johnson 2005) from those events where an individual MCS was responsible for the repeated passage of convection over a fixed location (the later would constitute the BB and TL/AS categories). The aforementioned distinctions between the two event types were based on a fixed precipitation duration threshold or the subjective determination of whether rainfall areas in radar imagery were composed of one or multiple MCSs. This introduces a nonnegligible degree of ambiguity into the event classification process, and there is no guarantee these subjectively determined distinctions define two dynamically different atmospheric phenomena.

Several previous authors have utilized rotated principal component analysis (RPCA; Schaefer and Doswell 1984; Jones et al. 2004; Mercer et al. 2012) as an objective method for sorting a sample of cases into subtypes based on their synoptic-scale atmospheric conditions (rather than their visual appearance in radar imagery). Composite analyses computed from such synoptic subtypes yield more specific information on the synoptic-scale features that drive the phenomena of interest, since events exhibiting similar synoptic states are *objectively* grouped together. In addition, they highlight key patterns of variability within the larger sample of events.

In this study, we apply RPCA to atmospheric fields associated with a large sampling of heavy-rain-producing MCSs to analyze the variability in synoptic-scale atmospheric fields associated with this MCS archetype, and to highlight the role of synoptic-scale processes in the quasi-stationary MCS behavior. This research sets the stage for several subsequent high-resolution numerical modeling studies that will comprehensively analyze the convective-scale dynamics of these MCSs. The organization of this paper is as follows. Section 2 outlines the results from RPCA on the atmospheric fields associated with the cases we selected. Composites of atmospheric fields for the resulting objectively identified synoptic subtypes are analyzed and compared in section 3, and radar reflectivity characteristics of these subtypes are cataloged and compared in section 4. Section 5 describes mechanisms for which the synoptic-scale environment contributed to the observed MCS behaviors in radar reflectivity, and our results are summarized and discussed within the context of the existing literature and ongoing/future work in section 6.

## 2. Statistical analysis of events

### a. Case selection

A database of heavy-rain-producing events was obtained by automatically searching daily gridded precipitation data from the National Oceanic and Atmospheric Administration/Climate Prediction Center (NOAA/CPC) Daily U.S. Unified Precipitation dataset (http://www.esrl.noaa.gov/psd/) for 24-h gridpoint precipitation accumulation totals exceeding 12.5 cm in a 24-h period between the years of 2002 and 2011 (this search yielded 401 events). The analysis was constructed from rain gauge observations in the continental United States, interpolated onto a 0.25° × 0.25° grid. The coarse resolution of this precipitation dataset (e.g., relative to stage IV precipitation, which is available on a 4 km × 4 km grid) served as an additional restricting criterion, whereby

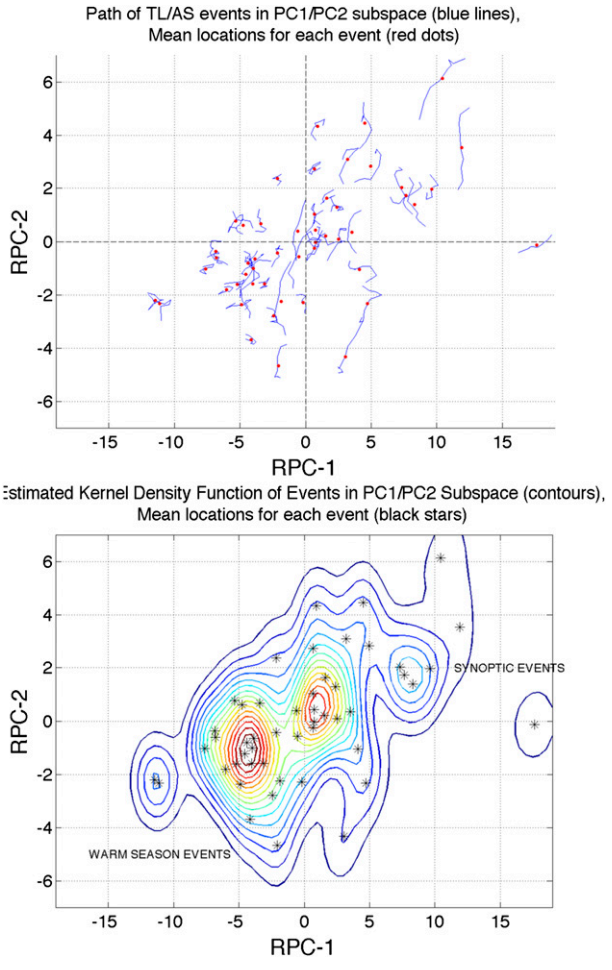


FIG. 2. (top) Scatterplot of the temporal mean RPC1 and RPC2 loadings over the 36 h of NARR data analyzed for each event (red stars), and the 18-h path of each event through the RPC1 and RPC2 subspace (blue lines). (bottom) Estimated kernel density function of atmospheric states in the RPC1 and RPC2 subspace over all events and all times (color contours), and the temporal mean RPC1 and RPC2 loadings over the 36 h of NARR data analyzed for each event (black stars). Synoptic-type events were defined in cluster analysis as those exhibiting a positive temporal mean RPC1 loading, while warm-season-type events exhibited a negative RPC1 loading (i.e., the RPC1 = 0 line divided case between each cluster). Note that synoptic-type events tended to also exhibit a positive RPC2 loading, and warm-season-type events tended to also exhibit a negative RPC2 loading.

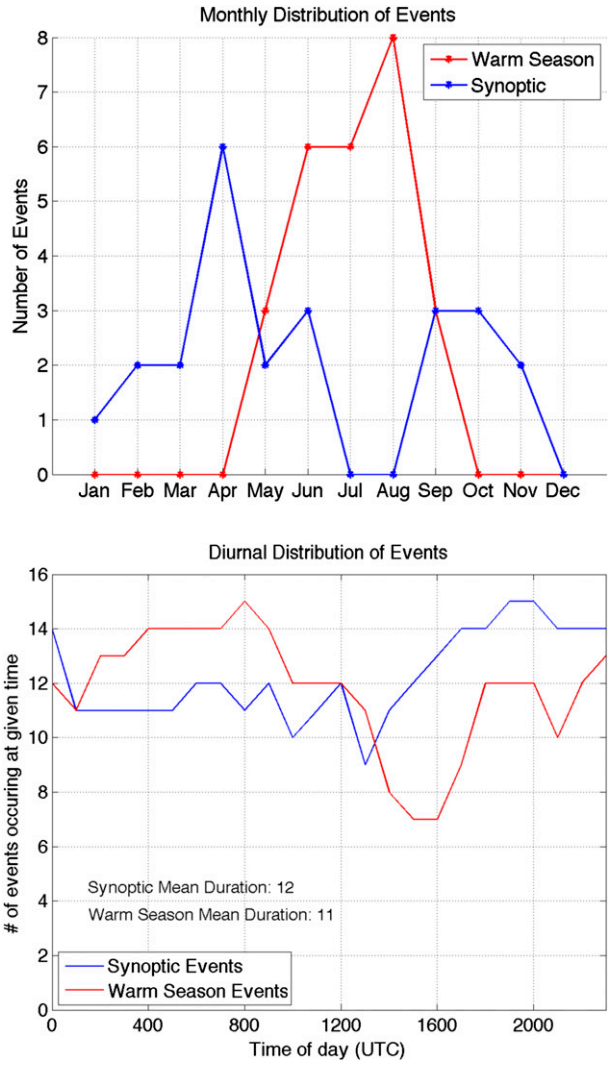


FIG. 3. (top) The seasonal frequency of synoptic-type (blue) and warm-season-type (red) events. (bottom) The diurnal frequency of synoptic-type (blue) and warm-season-type (red) events. The start time for each event was subjectively determined to be the time when the convection associated with the TL/AS system developed within, or moved into, the region of heavy rainfall accumulation, and the end time was subjectively determined to be when convection dissipated or left the region of heavy rainfall accumulation. An "event" was added to each 1-h bin if a TL/AS MCS was ongoing during that 1-h time frame.

highly localized heavy precipitation events (such as those produced by individual convective cells or slow-moving supercells) that may have produced over 12.5 cm at a few points on a fine grid did not produce sufficient rainfall on the coarse grid and were thereby intrinsically screened out.

We then subjectively examined Weather Surveillance Radar-1988 Doppler (WSR-88D) composite reflectivity from the National Center for Atmospheric Research–University Corporation for Atmospheric Research (UCAR) Mesoscale and Microscale Meteorology Division (MMM) image archive online (http://www.mmm.ucar.edu/imagearchive/) to identify cases where the heavy rainfall was produced by training of convection associated with an MCS. Rather than attempting to exclude "synoptic" and "backbuilding" type events from our database of events, we included all events where >50 dB$Z$ echoes persisted over the region of >12.5 cm of rainfall accumulation for 6 h or more, and

where a well-defined mesoscale convective vortex (MCV) was not present prior to the initiation of the convective system that produced heavy rain (defined as a localized midlevel cyclonic vorticity maxima that developed in association with a preceding MCS and lasted over 24 h). The idea was to keep the criteria for case selection very general, and to allow the statistical analysis to objectively classify subgroups. Note that another major difference in the methodology for case selection when compared to Schumacher and Johnson (2005) and other flash flood studies is the usage of a flat rainfall accumulation criterion rather than a recurrence interval criterion (thus removing any dependence on geography from the case selection process). This method identified 50 cases during this 10-yr period, which was a desirable number of cases for the subsequent statistical analysis (i.e., 50 cases was not a prohibitive number for computational purposes, and not too few as to preclude statistically robust results).

### b. RPCA

As discussed in section 1, a major caveat to the methodology of subjectively classifying convective morphology based on radar appearance is that a grouping of convective systems may have similar reflectivity characteristics, but exhibit notably contrasting governing dynamics and associated synoptic-scale environments. For instance, a composite analysis constructed from a grouping of events exhibiting considerable variability in the placement of a feature such as a low-level front would (in the composite analysis) likely reflect a much weaker temperature gradient than that of individual events due to the averaging involved in such a computation. Thus, the thermodynamic characteristics of the composite may exhibit little similarity to that of individual events. It is therefore advantageous to group subsets within the larger radar-reflectivity-based classification that exhibit similarities in their associated atmospheric fields, and generate a separate composite for each subset.

A simple objective approach to such event "grouping" is described by Mercer et al. (2012) within the context of tornado outbreaks, where principal component analysis (PCA) was applied to the atmospheric fields associated with a sampling of events, and a cluster analysis was subsequently performed in the subspace defined by the principal component (PC) responsible for the largest percentage of the variance in atmospheric fields among cases. The following section describes how we applied this statistical approach to our dataset in order to obtain composites of atmospheric fields for two synoptically distinct heavy-rain-producing MCS subtypes.

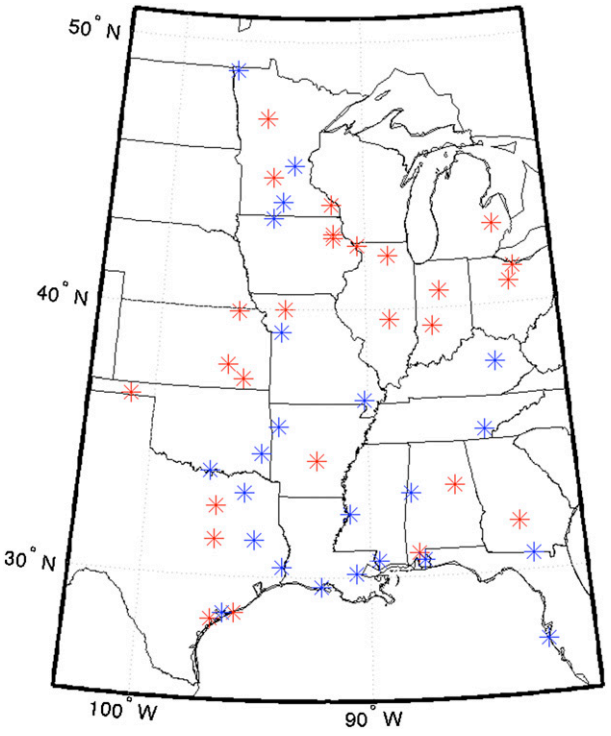


FIG. 4. Locations of event centroids for synoptic events (blue stars) and warm-season events (red stars). Starred locations correspond to the location where the maximum 1-h point precipitation accumulation value was observed for a given event.

For each of the 50 events, 3-hourly North American Regional Reanalysis (NARR; Mesinger et al. 2006) data were obtained at 3-h intervals for 15 h prior to 15 h after the time of the maximum 1-h point rainfall accumulation from the National Centers for Environmental Prediction (NCEP) stage IV precipitation accumulation analyses (Lin and Mitchell 2005). The NARR data were subsetted to a 51 × 51 gridpoint (1600 km × 1600 km) area centered at the location of the maximum 1-h accumulation. Following the approach of Mercer et al. (2012), the average of three-dimensional temperature, $U$ and $V$ wind components, mixing ratio, and geopotential height fields over all times and cases (i.e., the average was computed over $n \times m$ time frames on a given vertical level, where $n$ is the number of cases and $m$ is the number of time frames per case) were subtracted from these data, and variables were subsequently normalized at each vertical level by the standard deviation in space and time at that particular level. This standardization process transformed the 5 three-dimensional variables of interest into nondimensional data with a standard deviation of one, which exhibited consistent variability horizontally and vertically. (The climatological values of the nonstandardized data often exhibit considerable vertical variability, which is unfavorable for PCA.) The

TABLE 1. List of the cases used to generate composite analyses, their latitudes and longitudes, and synoptic subtypes. Locations correspond to the grid point in the stage IV precipitation analysis that experienced the maximum 1-h precipitation accumulation from the TL/AS MCS. Warm-season events are italicized.

| Date | Subtype | Lat (°N) | Lon (°W) | Date | Subtype | Lat (°N) | Lon (°W) |
|---|---|---|---|---|---|---|---|
| 3 Mar 2002 | Synoptic | 30.63 | 82.88 | 15 Sep 2004 | Synoptic | 43.88 | 94.63 |
| 19 Mar 2002 | Synoptic | 34.63 | 94.88 | 19 Oct 2004 | Synoptic | 35.05 | 87.81 |
| 8 Apr 2002 | Synoptic | 35.63 | 94.13 | 2 Nov 2004 | Synoptic | 28.63 | 96.38 |
| 11 Jun 2002 | Synoptic | 48.88 | 96.88 | 1 Apr 2005 | Synoptic | 30.63 | 87.63 |
| *23 Jun 2002* | *Warm season* | *47.13* | *95.13* | 4 Jun 2005 | Synoptic | 39.13 | 94.13 |
| *22 Aug 2002* | *Warm season* | *42.38* | *90.38* | *10 Aug 2005* | *Warm season* | *31.38* | *96.88* |
| 19 Oct 2002 | Synoptic | 33.13 | 95.63 | *25 Aug 2005* | *Warm season* | *37.88* | *96.63* |
| 21 Feb 2003 | Synoptic | 30.38 | 93.88 | 25 Sep 2005 | Synoptic | 44.00 | 89.63 |
| 7 Apr 2003 | Synoptic | 32.38 | 90.88 | 2 Jan 2006 | Synoptic | 27.38 | 82.63 |
| 8 Apr 2003 | Synoptic | 29.63 | 92.13 | *22 Jun 2006* | *Warm season* | *41.38* | *82.63* |
| 6 May 2003 | Synoptic | 35.38 | 84.63 | *8 Sep 2006* | *Warm season* | *31.88* | *83.38* |
| *8 May 2003* | *Warm season* | *33.38* | *86.13* | 23 Sep 2006 | Synoptic | 36.63 | 90.13 |
| *18 May 2003* | *Warm season* | *30.88* | *87.88* | 26 Oct 2006 | Synoptic | 31.38 | 95.13 |
| *12 Jun 2003* | *Warm season* | *34.38* | *92.38* | *19 Aug 2007* | *Warm season* | *43.91* | *91.69* |
| 25 Jun 2003 | Synoptic | 45.38 | 93.63 | *21 Aug 2007* | *Warm season* | *40.83* | *82.86* |
| *5 Jul 2003* | *Warm season* | *40.63* | *86.38* | *7 Sep 2007* | *Warm season* | *39.91* | *96.19* |
| *21 Jul 2003* | *Warm season* | *28.38* | *96.88* | *7 Jun 2008* | *Warm season* | *39.93* | *86.78* |
| *29 Aug 2003* | *Warm season* | *37.38* | *95.88* | *25 Jun 2008* | *Warm season* | *40.00* | *93.94* |
| *1 Sep 2003* | *Warm season* | *39.63* | *88.88* | 30 Apr 2009 | Synoptic | 33.91 | 97.19 |
| 28 Nov 2003 | Synoptic | 30.13 | 90.63 | *8 Aug 2009* | *Warm season* | *44.91* | *94.69* |
| 6 Feb 2004 | Synoptic | 33.13 | 88.13 | *9 Aug 2009* | *Warm season* | *43.00* | *83.44* |
| 26 Apr 2004 | Synoptic | 30.63 | 89.63 | *13 Jun 2010* | *Warm season* | *36.58* | *101.11* |
| *14 May 2004* | *Warm season* | *28.63* | *95.88* | *23 Jul 2010* | *Warm season* | *42.66* | *91.61* |
| 31 May 2004 | Synoptic | 37.88 | 83.88 | *24 Jul 2010* | *Warm season* | *42.00* | *88.86* |
| *29 Jul 2004* | *Warm season* | *32.63* | *96.88* | *28 Jul 2011* | *Warm season* | *42.83* | *91.61* |

data were then reshaped into a rectangular matrix $\mathbf{Z}$, with dimensions of $5NMK \times 11n$, where $N$ and $M$ are the numbers of grid points in the $X$ and $Y$ directions, respectively; $K$ is the number of vertical levels (the factor of 5 on $NMK$ results from there being five separate variables considered); and $n$ is the number of separate cases (the factor of 11 on $n$ results from there being an 11 time-frame progression for each case, since data are obtained for 15 h prior and 15 h after the time maximum rainfall accumulation at 3-h intervals in each case). The correlation matrix $\mathbf{R}$ of $\mathbf{Z}$ was computed using the formula

$$\mathbf{R} = \frac{1}{5NMK - 1}\mathbf{Z}^{\mathrm{T}}\mathbf{Z}. \tag{1}$$

The values in $\mathbf{R}$ correspond to spatial correlations between atmospheric time "snapshots" rather than temporal correlations between grid points (note that correlation values in $\mathbf{R}$ reflect correlations between atmospheric fields at different times from the same case, as well as correlations between cases). This choice (to compute spatial rather than temporal correlations) was optimal given that the goal here was to obtain objective comparisons between cases [see Richman (1986) and Mercer et al. (2012) for more in-depth discussions on the issue]. The decomposition of $\mathbf{Z}$ in terms of principal components is

$$\mathbf{Z} = \mathbf{F}\mathbf{P}^{\mathrm{T}}, \tag{2}$$

where $\mathbf{F}$ is a $5NMK \times 11n$ matrix of PCs and $\mathbf{P}$ is an $11n \times 11n$ matrix of PC loadings, or "scores" (Wilks 2006). In this case, $\mathbf{P}$ was obtained from the eigenvector decomposition of $\mathbf{R}$, where

$$\mathbf{R} = \mathbf{E}\mathbf{D}\mathbf{E}^{\mathrm{T}} \quad \text{and} \tag{3}$$

$$\mathbf{P} = \mathbf{E}\mathbf{D}^{1/2}, \tag{4}$$

where $\mathbf{E}$ is a matrix of the eigenvectors of $\mathbf{R}$ and $\mathbf{D}$ is a diagonal matrix of the singular values belonging to each eigenvector in $\mathbf{E}$. Note that PCs themselves need not be computed. We rather focus on the distribution of loadings in the vector subspace defined by the leading two principal components in our subsequent analysis.

### c. *Identification of TL/AS synoptic subtypes*

PC patterns are analogous to empirical orthogonal functions (EOFs) and they correspond to spatial patterns of variability within the atmosphere; for instance, two separate EOFs of a Northern Hemisphere sea level

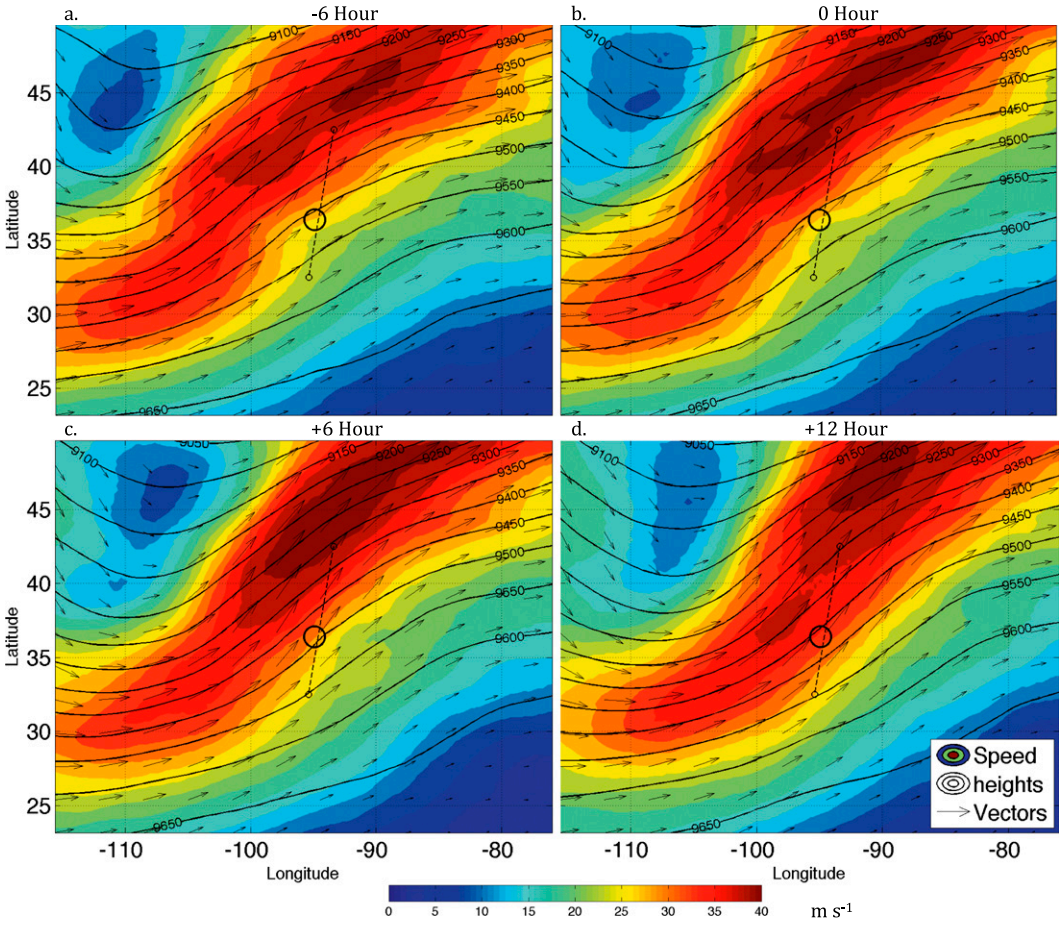


FIG. 5. The 18-h event-centered composite progression from 24 synoptic-type events of 300-hPa wind speed (m $s^{-1}$, shading), wind vectors (arrows), and geopotential height (black lines at intervals of 50 m) from (a) 6 h prior to, (b) the time of, (c) 6 h after, and (d) 12 h after peak 1-h rainfall accumulation was observed at the event location. A black circle at the center of each frame indicates the point location of maximum 1-h rainfall accumulation. The specific latitudes and longitudes shown are arbitrarily selected to illustrate the spatial scale. The dashed black line near the center of each panel shows the cross-sectional path in Fig. 13.

pressure time series correspond to the northern annular mode and the North Atlantic Oscillation, respectively, with a positive (negative) loading on each respective EOF indicating a positive (negative) phase of these patterns (Thompson and Wallace 1998). In the case of our analysis, principal components highlighted the most prominent spatial differences between our cases; that is, two cases with similar loadings on a particular principal component pattern exhibited more synoptic similarity to each other than two cases with substantially different loadings on that particular pattern. Principal components, by design, are ordered in the matrix **F** based on the magnitude of their contribution to the variance of the dataset. In practice, a small number of leading principal components often explain a large percentage of the variance of a time series, and the degrees of freedom within a dataset are substantially reduced by only considering the variability within the loadings of a few leading patterns.

The orientation of a particular eigenvector associated with a PC may not necessarily point in the local direction of maximum variability within a dataset, however, owing to the constraint of orthogonality (all cross correlations between PC loadings are necessarily zero). The orthogonality constraint is optimal when a particular analysis aims to isolate distinct dynamical processes between individual PCs (e.g., the identification of signatures of dynamically distinct teleconnection patterns); however, it has been shown that the practice of rotating loadings on a number of the leading PCs (rotated principal component analysis) by means of a linear transformation often results in spatial PC patterns that exhibit more realistic atmospheric structures (i.e., more physically interpretable) than PCs corresponding to

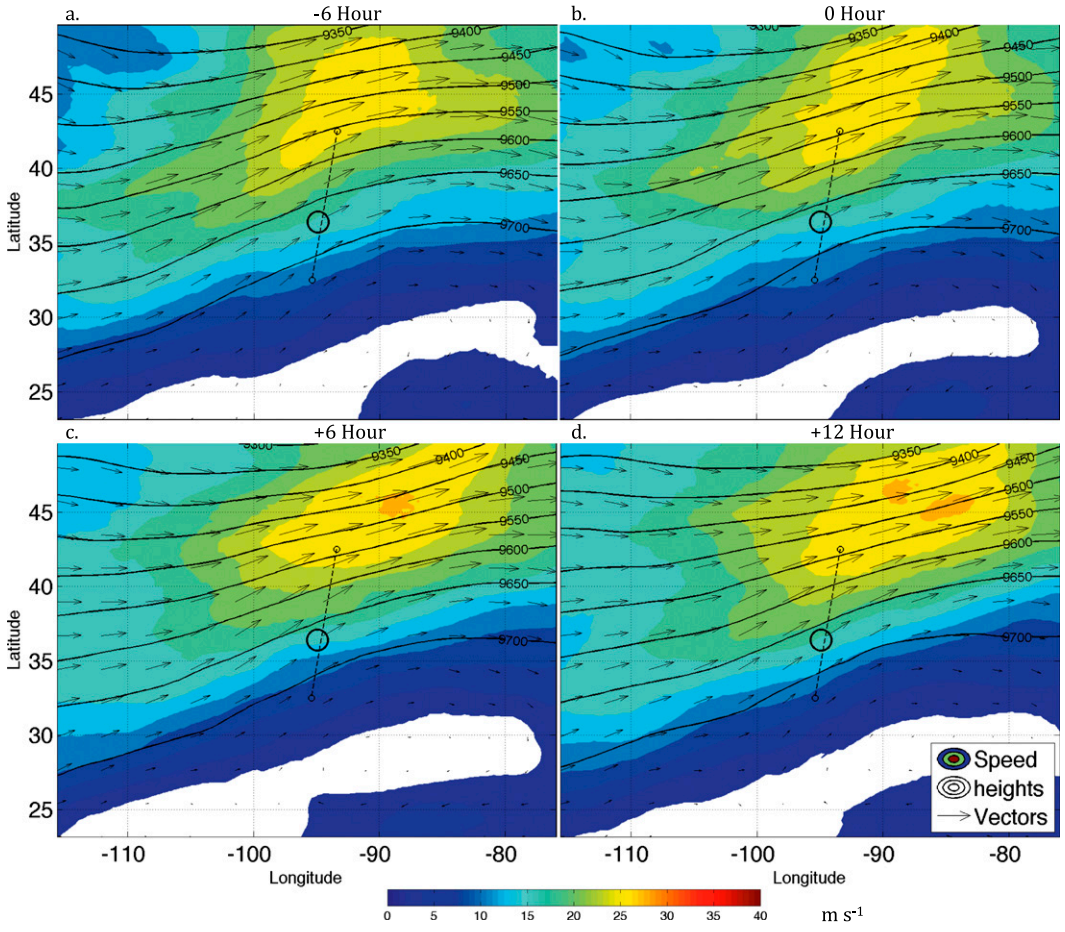


FIG. 6. As in Fig. 5, but for warm-season-type events. The cross-sectional path along the dotted line now corresponds to Fig. 14.

unrotated loadings [a more detailed discussion of this issue is provided by Richman (1986) and Mercer et al. (2012)]. We therefore performed a varimax rotation (Wilks 2006) on the leading 10 PC loadings of our data and obtained 10 new rotated PC loadings. Note that the ratios of the variance of the leading 4 PC loadings to the sum of the variance of the leading 10 PC loadings were 0.71, 0.11, 0.07, and 0.04, respectively, indicating that the leading rotated PC explained an overwhelming percentage of the total variance. Patterns within the subspaces defined by trailing PCS (e.g., PCs 3, 4, 5, etc.) were also examined; they were ultimately excluded from the case selection analysis due to the lack of coherent multimodalities within their subspaces.

We then analyzed scatterplots of loadings of our cases in the rotated PC1–PC2 (RPC1–RPC2) subspace (Fig. 2, top). It was immediately evident that the RPC1–RPC2 loadings did not change considerably for most cases over the 30-h time progressions considered, since the blue lines are short relative to the expanse of the phase space, and do not stray far from the average value over that time period. We therefore considered only the 30-h time-average RPC loadings for each case, which greatly reduced computation times by reducing the number of data points from 550 to 50. The estimated probability density function of these states (Fig. 2, bottom) revealed two pronounced event population maxima within the subspace, with local maxima in the upper-right and lower-left quadrants (relative to the origin), along with several less pronounced local maxima (note that since most of the less pronounced maxima consisted of one or two events, their sample size was insufficient for them to be considered separately from the more populated local maxima). A less coherent bimodal distribution was also evident in the unrotated PC1–PC2 subspace (not shown). Later in this section, we describe how the results from RPCA are used to generate synoptic composites for two TL/AS subtypes. Composites computed from RPCs exhibited substantially greater differences between the two synoptic subtypes than those computed

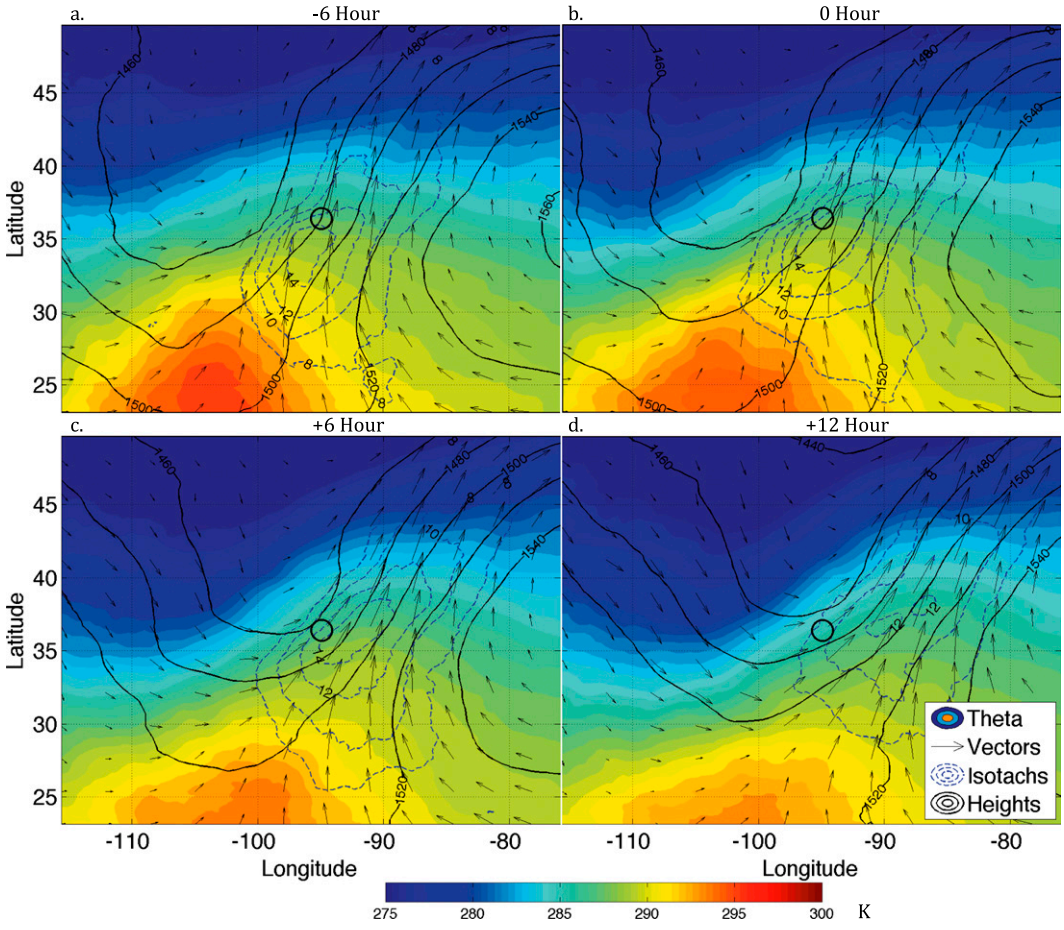


FIG. 7. The 18-h event-centered composite progression from synoptic-type events of 850-hPa potential temperature (K, shading), wind speed (blue dashed contours at intervals of 2 m s$^{-1}$, starting at 8 m s$^{-1}$), wind vectors (black arrows), and geopotential height (black lines at intervals of 20 m). Panel times are the same as those in Fig. 5. A black circle at the center of each frame indicates the point location of maximum 1-h rainfall accumulation. The specific latitudes and longitudes shown are arbitrarily selected to illustrate the spatial scale.

from unrotated PCs, which served as an a posteriori justification for the usage of RPCs in our analysis hereafter (i.e., RPCs provided a more coherent separation into distinct subtypes).

There are various methods for objectively identifying groupings, or ''clusters'' within a distribution of points in two-dimensional space (i.e., the RPC1–RPC2 loadings). We followed the methodology of Mercer et al. (2012) and performed *k*-means cluster analysis (Wilks 2006) in the RPC1–RPC2 subspace. This method utilizes an iterative algorithm to fit the data into a prespecified number of clusters (assuming each datum only belongs to one cluster). Though additional objective algorithms are typically utilized in order to determine the optimal number of clusters (Mercer et al. 2012) prior to *k*-means cluster analysis, we circumvented this step and subjectively specified that the algorithm fit to two clusters ($k = 2$, $k$ being the number of clusters), given the bimodality evident in Fig. 2. Cases were flagged with a 1 (24 events) or 2 (26 events) based on which cluster they belonged to, and composites of NARR atmospheric fields were subsequently computed for each cluster. We also performed *k*-means cluster analysis with the data fit to more than two clusters ($k > 2$), and compared the results (not shown) to the analysis presented in this paper. Clusters 2 and 3 from the $k = 3$ solution yielded nearly identical atmospheric composites to one another, and solutions for $k > 3$ yielded additional clusters composed of only one or two events (i.e., their presence was highly sensitive to sampling).

Note that while we refer to RPCA as an ''objective'' method, contrasted with ''subjective'' case sorting, we must note that (as with most statistical methods), there remain subjective ''choices'' to be made through the execution of the method (e.g., number of PCs to consider for cluster analysis, number of clusters to fit the

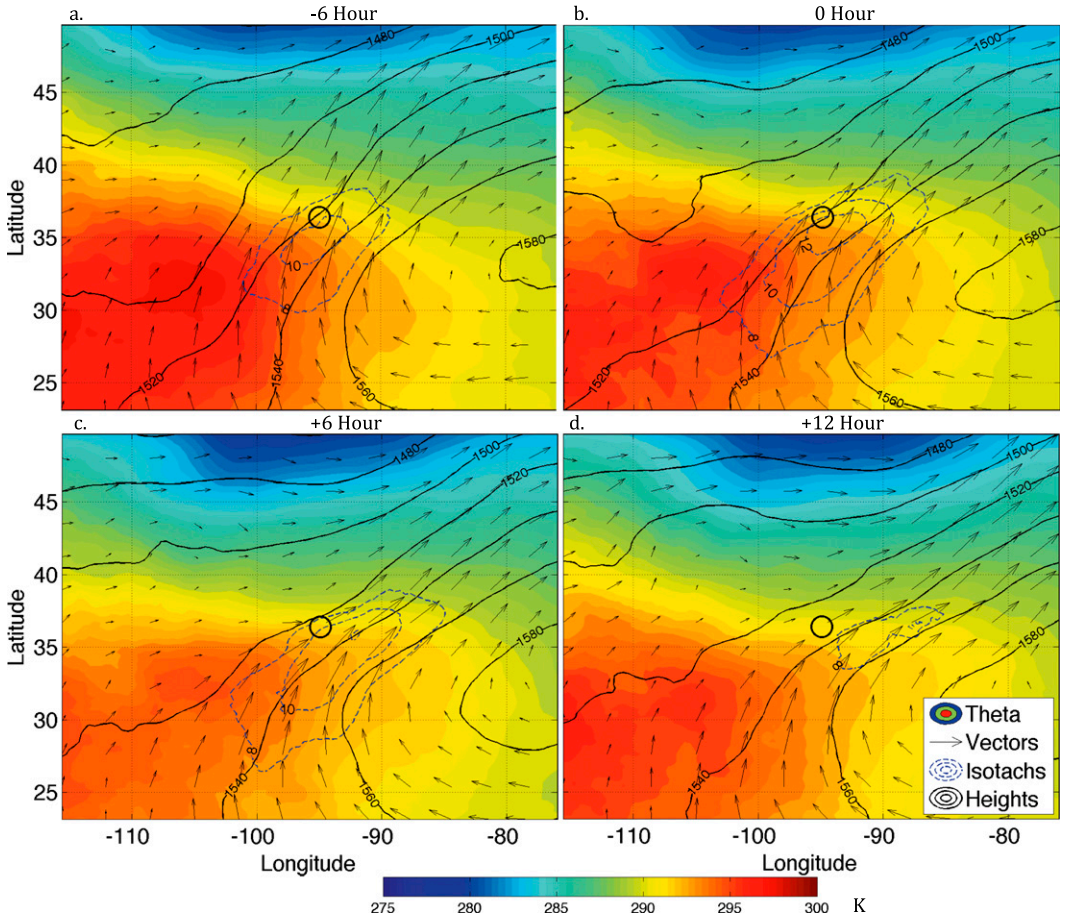


FIG. 8. As in Fig. 7, but for warm-season-type events.

data to). The RPCA method does, however, dramatically reduce the role of such subjective choices in case selection over fully subjective methods and, thereby, dramatically decreases the degrees of freedom involved.

## 3. Composites of synoptic subtypes

As will be illustrated later in this section, the most notable differences in composite atmospheric fields between cluster-1- and cluster-2-type events were evident between their upper-level jet and low-level thermodynamic structures. Cluster 1 events occurred downstream of a progressive upper-level trough and featured a classic low-level cyclone structure with a well-defined low-level trough, trailing cold front, and preceding warm front. They were subsequently termed synoptic subtype events due to their association with the aforementioned features. Cluster 2 events occurred within the right-entrance region of a low-amplitude anticyclonically curved upper-level jet streak, and only exhibited a discernable warm front at low levels. They were termed warm-season subtype events since the aforementioned synoptic-scale environment is more characteristic of the North American summertime (see Fig. 2 for the locations of these subtypes within the RPC1–RPC2 subspace). The seasonal frequencies of these events (shown in Fig. 3) were sharply contrasted between the two subtypes, with synoptic-type events frequently occurring in the spring and fall months (when high-amplitude troughs are more frequent), and warm-season events being predominantly confined to the summer months. The warm-season cases exhibited a diurnal peak in frequency during the overnight and early morning hours (~0300–0900 UTC), while synoptic-type events exhibited a diurnal peak in frequency during the afternoon and evening hours (~1700–0100 UTC; Fig. 3). Note that the association of warm-season heavy rainfall events with the nocturnal jet maximum is well established in the previous literature on MCSs, mesoscale convective complexes (MCCs), and heavy convective rainfall (e.g., Pitchford and London 1962; Maddox et al. 1979, Maddox 1980, 1983; Augustine and Caracena

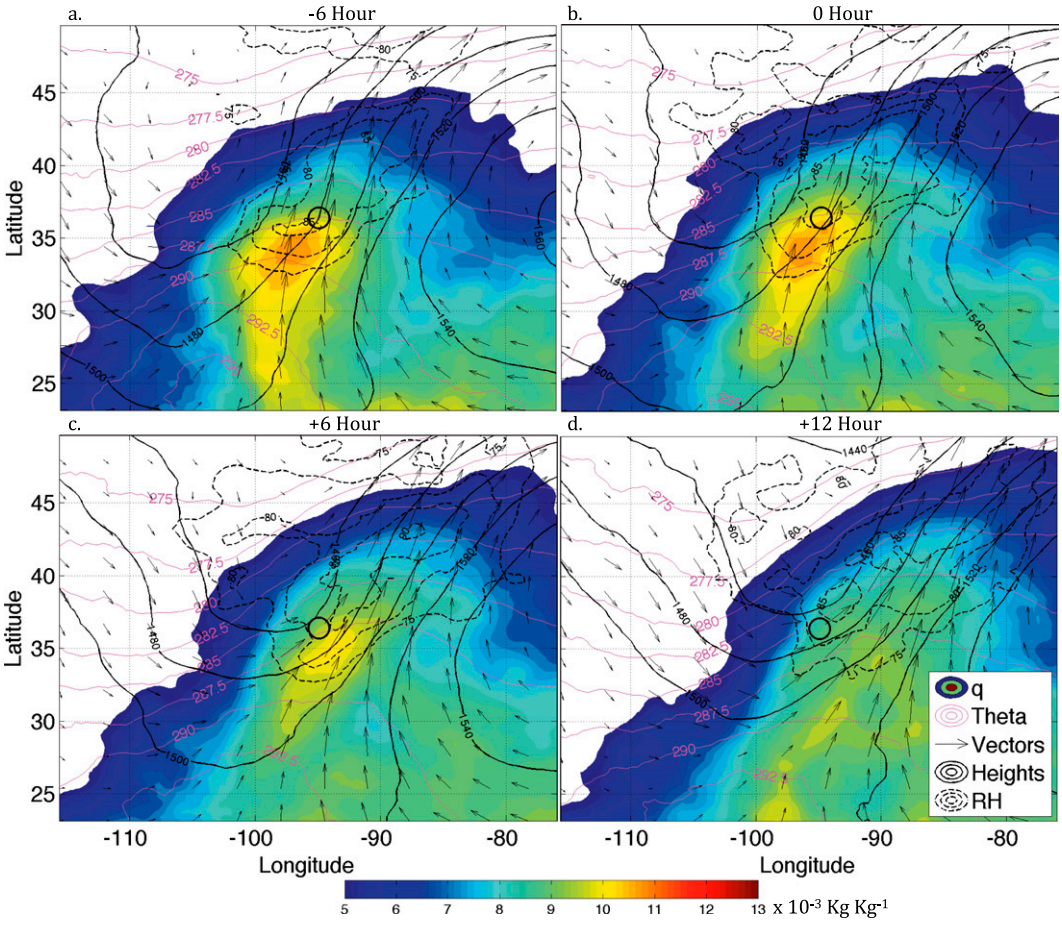


FIG. 9. The 18-h event-centered composite progression from synoptic-type events of 850-hPa mixing ratio (shading, $\times 10^{-3}$ kg kg$^{-1}$), relative humidity (%, black dashed contours at intervals of 5% starting at 75%), wind vectors (black arrows), geopotential height (black lines at intervals of 20 m), and potential temperature (K, magenta contours). Panel times are the same as those in Fig. 5. A black circle at the center of each frame indicates the point location of maximum 1-h rainfall accumulation. The specific latitudes and longitudes shown are arbitrarily selected to illustrate the spatial scale.

1994; Moore et al. 2003; Schumacher and Johnson 2005; Tuttle and Davis 2006; Monaghan et al. 2010). A comparison of the spatial distribution of events between the two subtypes (Fig. 4) shows a slight northward preference for warm-season events relative to synoptic-type events, which is intuitively consistent with the time of the year when the ingredients for convection more frequently reach the north-central United States. Note also that both event types were restricted to regions east of the Rocky Mountains and west and south of the Appalachian Mountains (no geographical constraint was imposed during the case selection process). Table 1 indicates which synoptic subtype each of the cases considered in this study belongs to.

Upper-level features associated with synoptic-type events were more zonally progressive than those corresponding to warm-season-type events, with the upper-level trough axes in synoptic-type events having moved from ~112° to 105°W in 18 h (Fig. 5), whereas little discernable zonal translation of upper-level features occurred in warm-season events (Fig. 6). Although both event types remained within the right-entrance region of an upper-level jet streak throughout the 18-h evolution, 300-hPa peak wind speeds associated with the composites of synoptic-type events were considerably stronger (~40–45 m s$^{-1}$) than those associated with warm-season-type events (~25–30 m s$^{-1}$). This is consistent with a climatologically stronger jet in the spring and fall months compared with the warm season over the United States.

Both event types occurred within a generally east–west-oriented temperature gradient at the northern nose of a southerly low-level jet, with warm air to the south

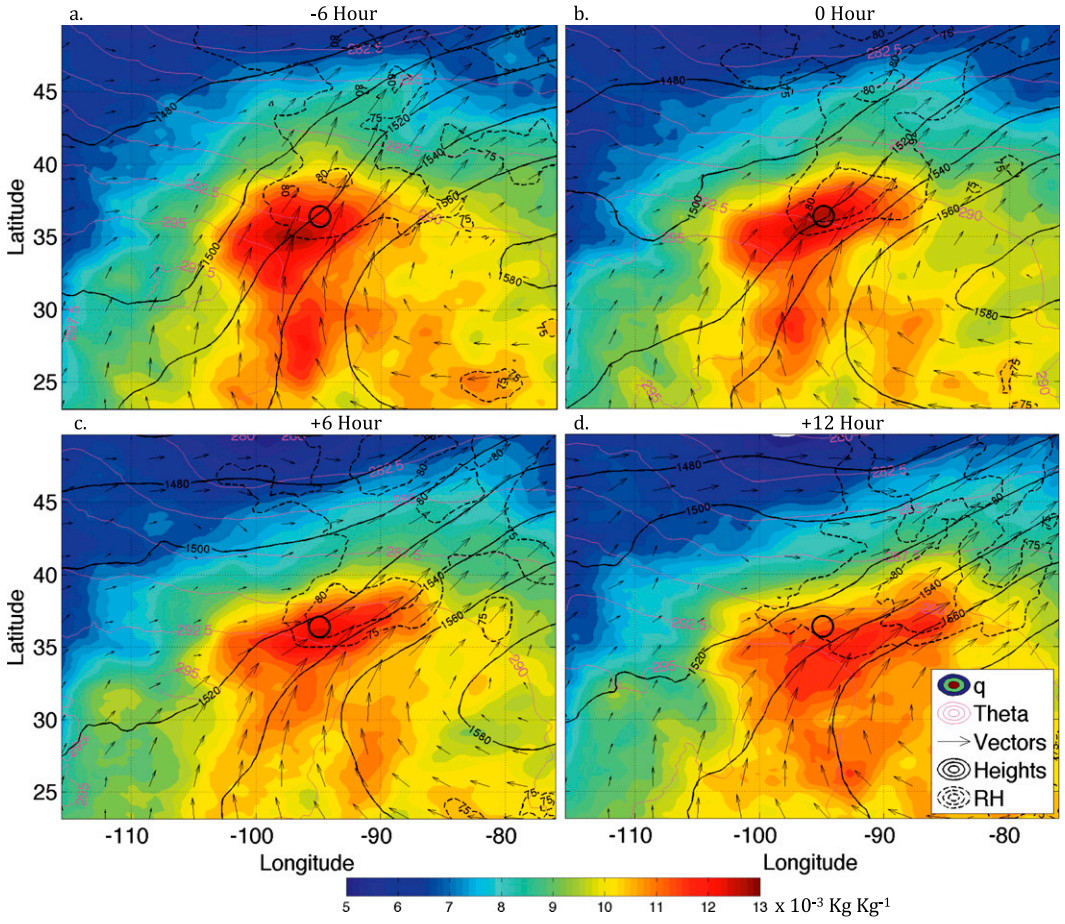


FIG. 10. As in Fig. 9, but for warm-season-type events.

(Figs. 7 and 8). The axis of warm air in synoptic-type events initially resided to the south and southwest of the MCS location, and translated to the southeast of the event location through time. A cooler air mass that was initially to the west slowly progressed eastward during the 18-h period, eventually reaching the event location (Fig. 7). Warm-season-type events, on the other hand, featured a broader warm axis to the south, southwest, and west of the event location, with cooler air having remained far separated to the north of the event location (Fig. 8). Note that the low-level jet in warm season cases reached maximum intensity at the time of peak rainfall, and weakened considerably 12 h after peak rainfall, suggesting that the jet intensity was influenced by the diurnal boundary layer heating–cooling cycle. This may explain why warm season events exhibit a peak diurnal frequency during the overnight hours, which coincides with the diurnal maximum in jet strength. In contrast, the low-level jet in synoptic-type events remained at roughly the same intensity through the 18-h progression of rainfall, suggesting that the jet strength here was predominantly regulated by the low-level horizontal pressure gradient.

Both event types featured a persistent supply of low-level moisture to the event location by southerly inflow (Figs. 9 and 10). Warm-season-type events featured considerably more low-level moisture than synoptic-type events, though low-level temperatures in warm-season-type events were also warmer (and thus the spatial expanse of near-saturated relative humidity values was smaller for warm-season events).

The stronger winds aloft and more persistently strong low-level jet in synoptic-type events compared with warm-season-type events suggested that synoptic-type events also featured stronger large-scale forcing for ascent. Both event types occurred within a persistent, locally maximized region of low-level warm-air advection, though this region was much broader and exhibited greater peak values in the case of synoptic-type events (Figs. 11 and 12); this may partially explain why synoptic-type MCSs tend to exhibit greater spatial extent than warm season MCSs (an attribute that is discussed in

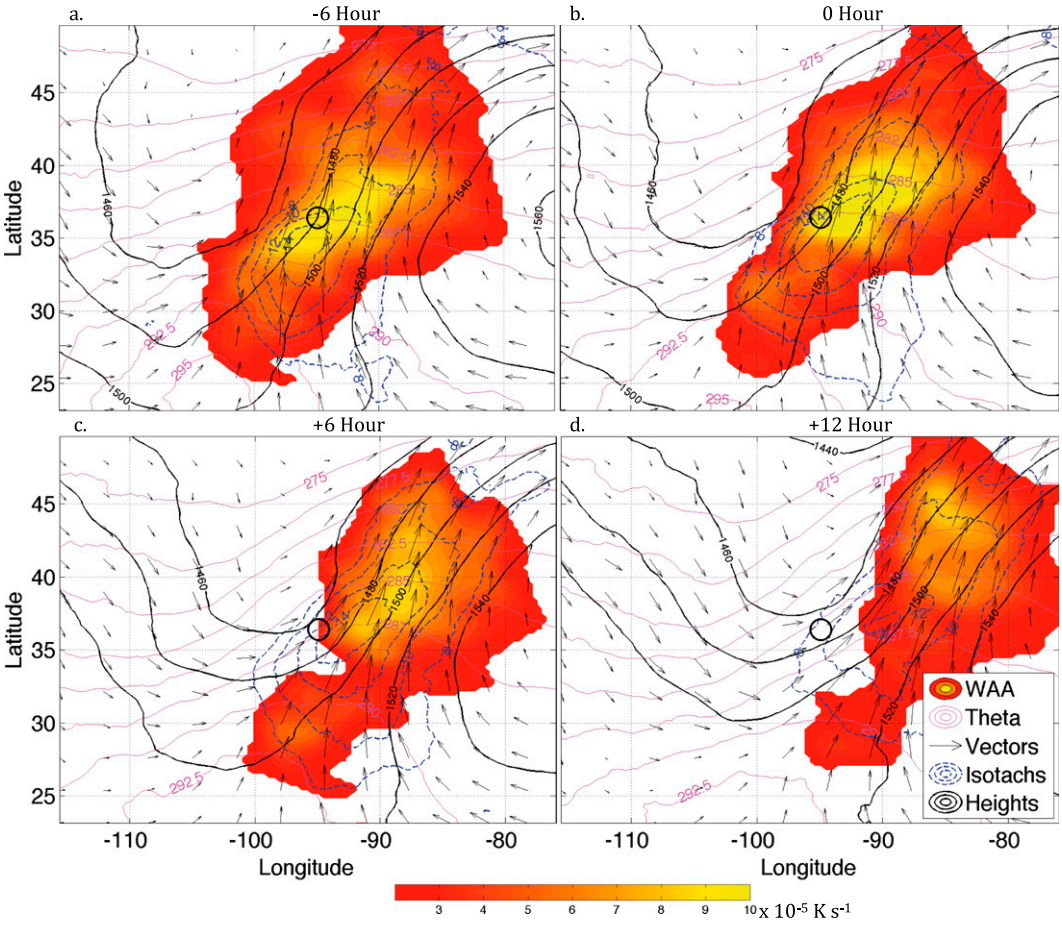


FIG. 11. The 18-h progression from synoptic-type events of 850-hPa potential temperature advection ($\times 10^{-5}$ K s$^{-1}$, shading; values below $2 \times 10^{-5}$ K s$^{-1}$ have been removed; derivatives were computed from composite atmospheric fields), wind speed (blue dashed contours at intervals of 2 m s$^{-1}$, starting at 8 m s$^{-1}$), wind vectors (black arrows), geopotential height (black lines at intervals of 20 m), and potential temperature (K, magenta contours). Panel times are the same as those in Fig. 5. A black circle at the center of each frame indicates the point location of maximum 1-h rainfall accumulation. The specific latitudes and longitudes shown are arbitrarily selected to illustrate the spatial scale.

greater detail in the next section). South–north vertical cross sections show an upward slope in isentropes at low levels in both case types (Figs. 13 and 14), which in conjunction with the generally southerly low-level flow, is illustrative of warm-air advection (note that upsloping isentropes were present throughout the depth of the troposphere in synoptic cases). Both case types also exhibited locally maximized low-level convergence and frontogenesis [which has been associated with nocturnal MCSs, Augustine and Caracena (1994); Junker et al. (1999); Moore et al. (2003); Galarneau et al. (2010)] along the nose of the low-level jet, locally maximized upper-level divergence within the right-entrance region to the upper-level jet streak, and maximized ascent between the convergent and divergent regions (Figs. 13 and 14). Convergence, divergence, and ascent magnitudes, as well as the north–south expanse of these quantities were considerably greater in synoptic-type events than in warm-season-type events. Although warm-season events exhibited considerably greater low-level moisture than synoptic-type events (Figs. 9 and 10), the expanse of near-saturated air parcels was greater for synoptic events due to low-level temperatures also having been greater in the case of the former (and saturation mixing ratios subsequently higher).

To obtain a sense of the variability of individual cases about the composite images examined earlier in this section, we computed the standard deviation of representative atmospheric fields at each grid point within our domain over synoptic and warm season cases:

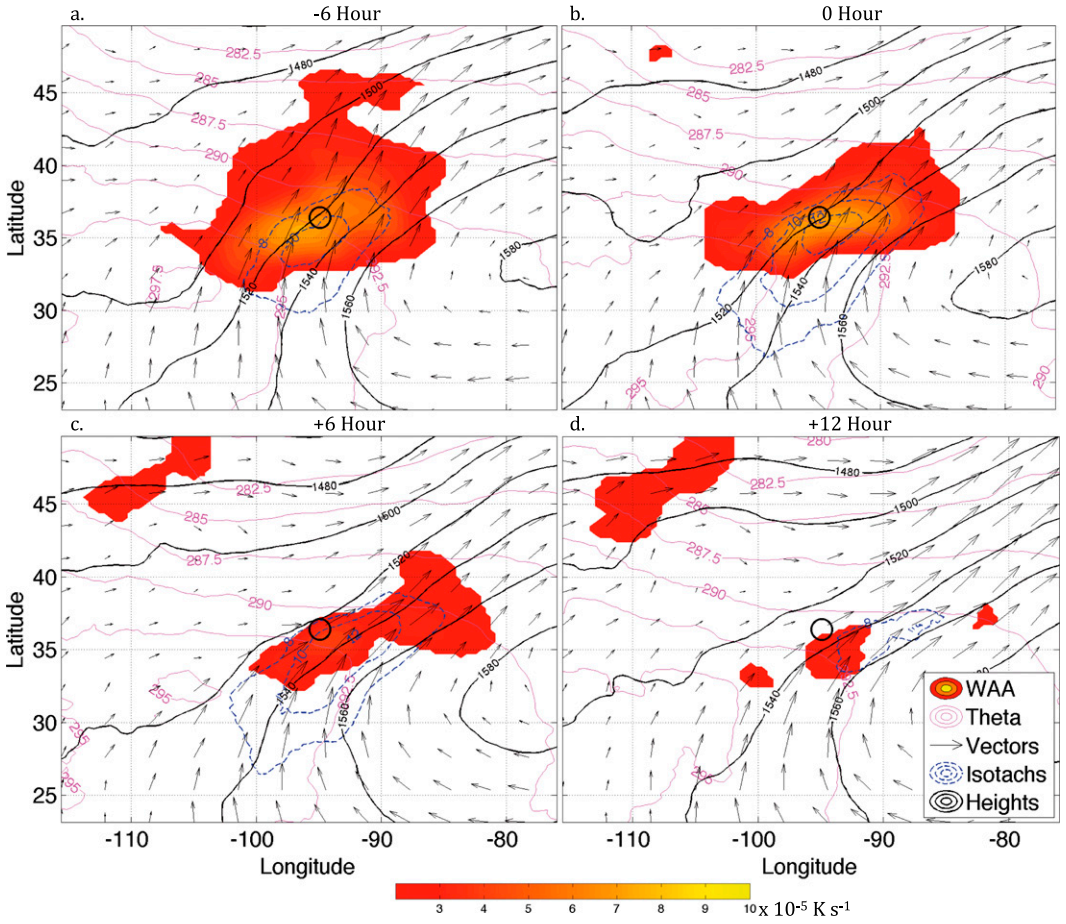


FIG. 12. As in Fig. 11, but for warm-season-type events.

$$\sigma_f(x,y,p,t) = \sqrt{\frac{1}{n-1}\sum_{i=1}^{n} f(x,ym,z,t,c_i)}, \qquad (5)$$

where $f$ is any arbitrary atmospheric field, $n$ is the number of either warm season or synoptic cases (depending on which event type we were computing the standard deviation quantity for), $t$ is the time removed from peak stage IV 1-h rainfall, and $c_i$ is a case number. Example maps of the 850-hPa wind speed and direction standard deviations are shown in Fig. 15. Note that synoptic events exhibit considerably greater standard deviation in wind speed through the low-level jet region (~6–7 m s$^{-1}$) than warm-season events (~3.5–4.5 m s$^{-1}$) (this is consistent with the greater degree of variability apparent associated with the synoptic-type event cluster in the RPC1–RPC2 subspace). Additional fields analogous to those depicted in Fig. 15 were examined (not shown), and exhibited spatial patterns of variance similar to those evident in the wind speed variability figures (as well as greater variance within synoptic fields over warm-season fields). Interestingly, the variability of wind direction within the low-level jet region is comparable between the two event types; in fact, the southwesterly direction of the low-level jet seems to be a fixture of all events (with a standard deviation of only 10°–25° in wind direction within the low-level jet between the two case types).

## 4. Radar reflectivity and precipitation accumulation area characteristics

We subjectively analyzed composite radar reflectivity imagery (warm-season events, Fig. 16; synoptic events, Fig. 17) to determine whether the two synoptic subtypes presented in this work exhibited notable differences in their salient radar features in addition to the differences in synoptic-scale atmospheric fields discussed in section 3.

Representative composite radar reflectivity images for three synoptic-type events show that training convection often developed as a broken line of individual

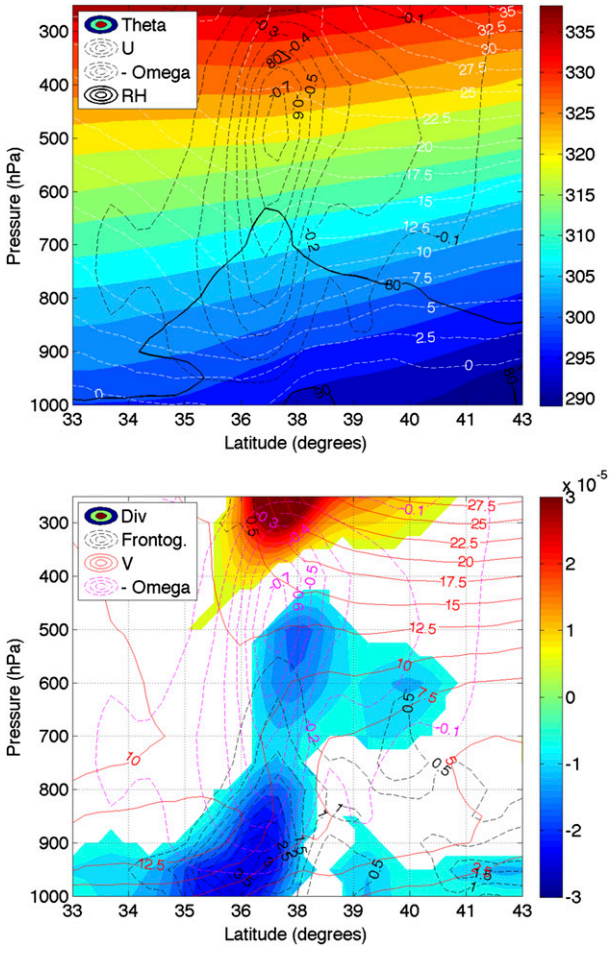


FIG. 13. Cross sections through the dotted line in Fig. 5 for synoptic-type events, at the time of maximum 1-h rainfall accumulation. (top) Potential temperature (K, shading), zonal wind velocity ($m\,s^{-1}$, white dotted contours), negative pressure vertical velocity ($Pa\,s^{-1}$, dotted black contours), and relative humidity (%, solid black contours). (bottom) Horizontal divergence ($\times 10^{-5}\,s^{-1}$, shading), negative pressure vertical velocity ($Pa\,s^{-1}$, dotted magenta contours), meridional wind speed ($m\,s^{-1}$, solid red contours), and horizontal frontogenesis ($K\,s^{-1}$, dotted black contours, $\times 10^{10}$).

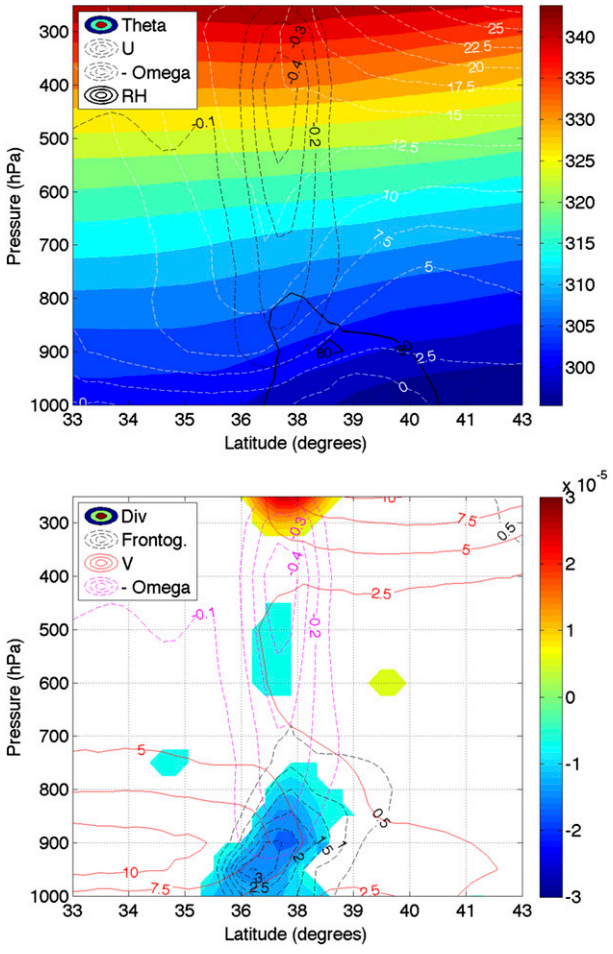


FIG. 14. As in Fig. 13, but for warm-season-type events.

convective cells (Fig. 16) along a nearly stationary warm front (less commonly, a slow-moving cold front). Initial convection then evolved upscale into a linear MCS within 1–5 h, with the motion of individual convective cells paralleling the linear convective region. The areal extent of synoptic-type MCSs was often highly elongated in the direction of the convective line, with a very high aspect ratio of convective line "length" to stratiform precipitation "width" (this is evident in radar images of all three events in Fig. 16). Thus, in many cases the length of the training line was sufficient so that predominantly line-parallel motion would bring an extended period of convective rainfall to a particular region without the line regenerating (i.e., backbuilding) upstream. Cessation of training convection was often accompanied by the passage of a progressive cold front and a progressive trailing-stratiform- (TS; e.g., Houze et al. 1989, 1990; Parker and Johnson 2000) type squall line; this is evident in the right panel of Fig. 16 for the case occurring on 15 September 2004 (though a trailing TS squall line occurred in all three of the cases shown in this figure).

The radar reflectivity presentations of synoptic-type events suggest that the aspect ratios (and overall sizes) of these events were often larger than those for warm-season events (this is somewhat evident when comparing radar imagery in Figs. 16 and 17). This is further supported by Fig. 18, which shows precipitation accumulation composites for both event types. Synoptic events exhibited greater areas of 20 mm of rainfall accumulation than warm-season-type events, though maximum precipitation accumulation values within the warm-season composite were greater than the analogous quantity for synoptic-type events. The average precipitation accumulation value through the composite

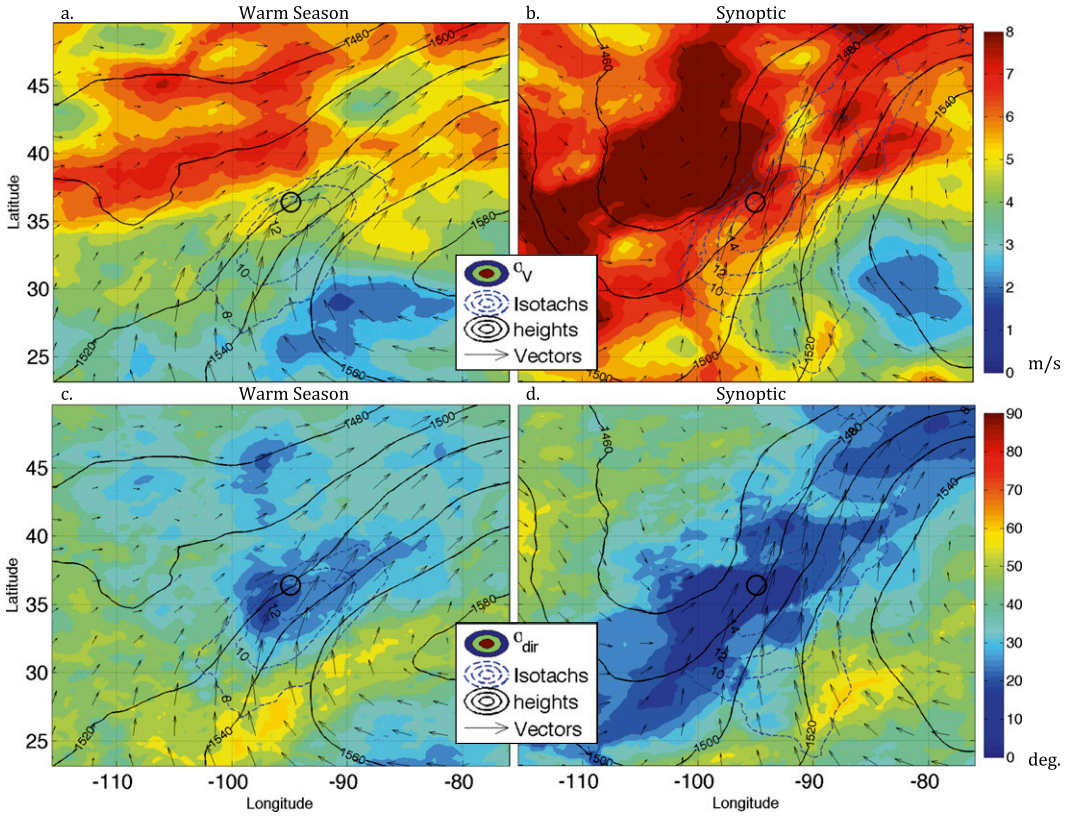


FIG. 15. Plots of the standard deviation [$\sigma$, see Eq. (5) in the text] of 850-hPa wind speed for (a) warm-season (shading, m s$^{-1}$) and (b) synoptic (shading, m s$^{-1}$) events, as well as (c) the standard deviation of wind direction for warm season (shading, °) and (d) synoptic (shading, °). Geopotential height (solid black contours, m, at intervals of 40 m), wind vectors (black arrows), and wind speed (blue dotted contours, m s$^{-1}$ starting at 8 m s$^{-1}$ and at intervals of 2 m s$^{-1}$) are shown in all panels. All panels are valid at the time of maximum 1-h rainfall accumulation from stage IV precipitation analysis. A black circle at the center of each frame indicates the point location of maximum 1-h rainfall accumulation. The specific latitudes and longitudes shown are arbitrarily selected to illustrate the spatial scale.

domain for synoptic-type events was 24.6 mm, while the analogous quantity for warm-season-type events was 16.6 mm. These statistics show that warm-season events tend to produce less expansive, but more concentrated precipitation areas than synoptic-type events, while the total precipitation production in synoptic-type events tends to be greater.

Initial development of convective cells associated with warm-season events often occurred to the rear of a progressive TS-type MCS, north of a slow-moving warm frontal boundary. Interestingly, this rear development in the wake of a TS-type MCS passage often occurred well north of the implied gust front at the southern periphery of the cold pool produced by the initial MCS (see radar imagery of the 22 August 2002 and 25 August 2005 cases in Fig. 17); we will hereby refer to this phenomena as rearward off-boundary development (ROD). In some cases ROD occurred to the rear of a well-defined bowing-line segment, akin to the "bow and arrow" phenomena described by Keene and Schumacher (2013), while in other cases the initial progressive MCS was less organized, and did not exhibit bowing-line segments. Our initial analysis of several real-data and idealized numerical simulations (which is not discussed here but will be comprehensively analyzed in future studies) suggests that similar dynamical processes to those described by Keene and Schumacher (2013) are responsible for the ROD events observed in our cases. Prolonged regeneration of convection on the upstream side of the MCS occurred in almost every warm-season case (in contrast to the synoptic-type events), which resulted in the upstream flank of the MCS remaining quasi stationary (see Corfidi 2003; Schumacher and Johnson 2005, 2006; Schumacher 2009).

To quantify the degree to which each TL/AS MCS subtype exhibited the characteristics that have been discussed in this section, the radar reflectivity features present in each case were subjectively cataloged. We

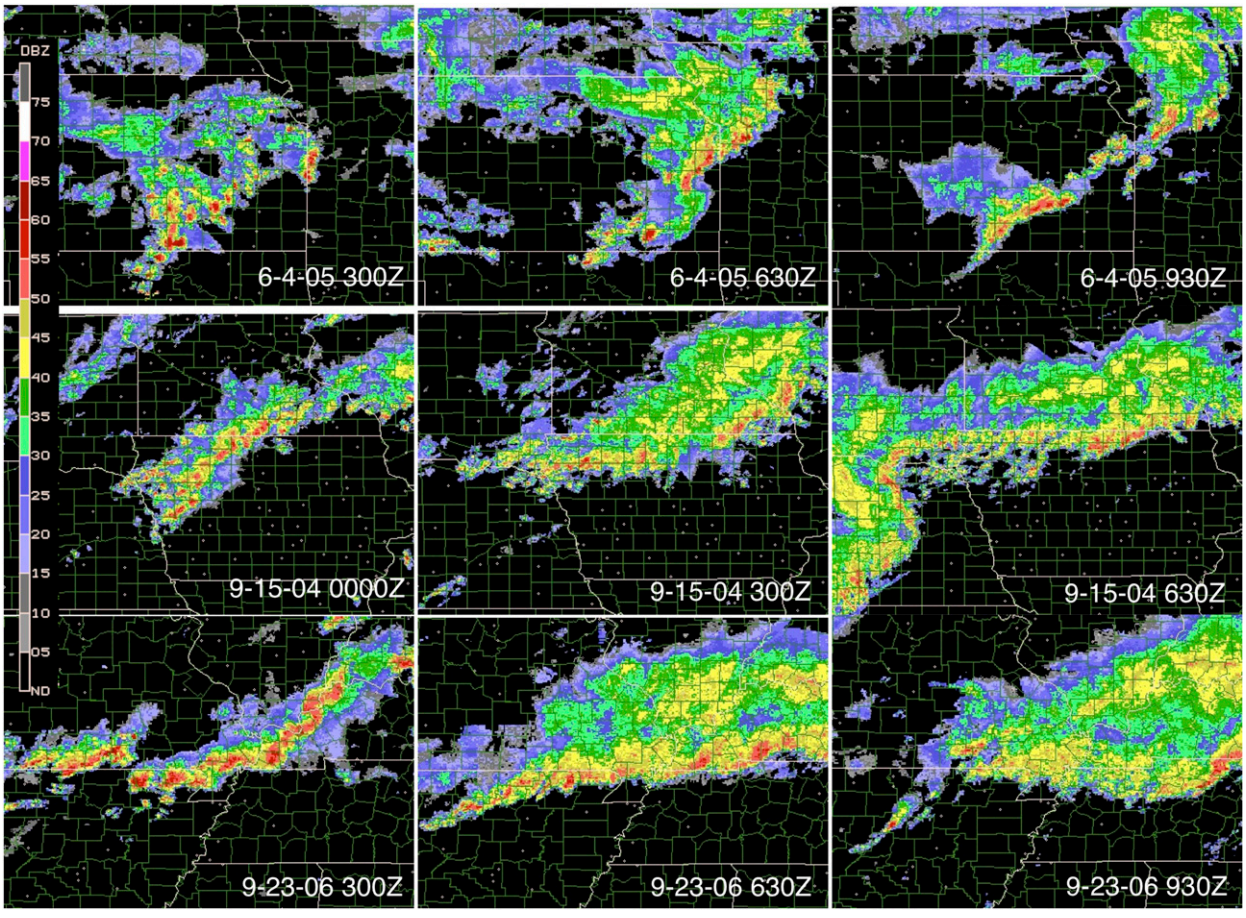


FIG. 16. Composite radar reflectivity images from three different synoptic-type events. Dates and times for each image are listed in the bottom-right corner.

specifically noted whether the MCS occurred along a warm, cold, or stationary surface front; whether an initial or trailing progressive MCS was present; and whether ROD occurred. If a particular event occurred along a frontal boundary, the boundary was typically very slow moving; thus, difficulties arose in distinguishing warm–cold fronts from truly stationary fronts. Surface boundaries were therefore considered stationary if there was little-to-no cross-boundary component of surface flow (i.e., near-zero surface temperature advection). Roughly half of the cases occurred along warm fronts, and only around of fifth occurred along cold fronts or fully stationary fronts. Figure 19 summarizes the prevalence of these properties between both MCS subtypes. Initial progressive MCSs prior to the onset of training convection were far more frequent in warm-season-type cases than synoptic-type cases, while trailing progressive MCSs following the training of convection were far more frequent in synoptic-type cases than warm-season-type cases. The ROD phenomena occurred in 50% of warm-season-type cases, and in none of the synoptic-type cases. The prevalence of these phenomena in warm-season cases is not surprising, considering the 850-hPa composites for warm-season-type cases shown in Fig. 8 are very similar to the composites computed exclusively from bow-and-arrow cases shown in Keene and Schumacher (2013).

## 5. Synoptic-scale factors contributing to observed radar reflectivity evolutions

An important fixture in the composite progressions for both subtypes is that the synoptic-scale features *continuously* supplied the ingredients for organized convection to the location where heavy rainfall events occurred through most of the 18-h time progression. These ingredients included moisture and conditional instability within southerly system-relative inflow, persistent synoptic-scale lifting, which included convergence

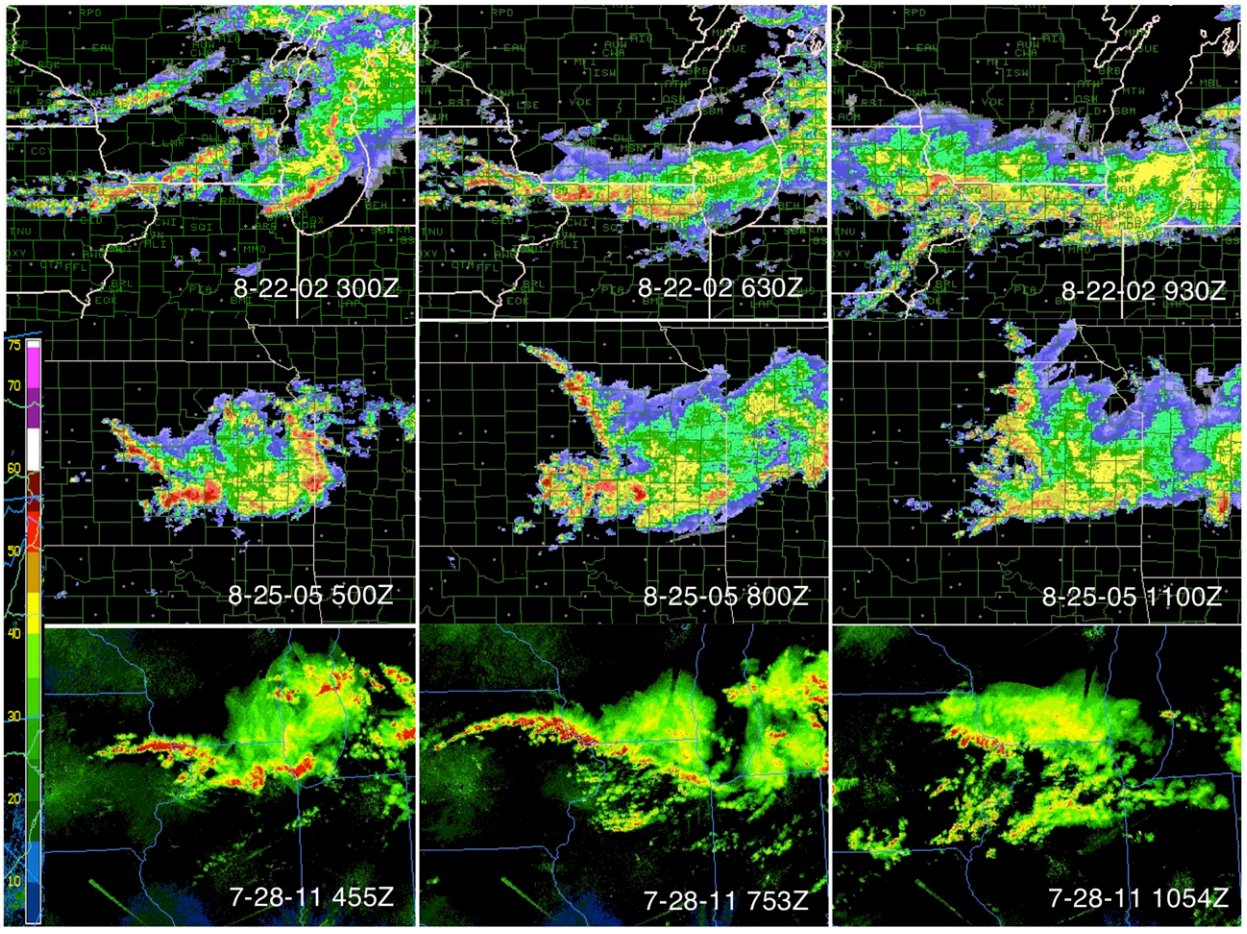


FIG. 17. As in Fig. 16, but for warm-season-type events. The color-scale top two events correspond to the color bar in Fig. 16; the color scale of the bottom event corresponds to the color bar on the bottom left.

and isentropic upglide along the nose of a low-level jet, frontogenetic lift along a quasi-stationary frontal boundary, and divergence within the right entrance region to an upper-level jet streak.

Additional aspects of the vertical wind profile in the MCS region may have also promoted quasi-stationary MCS behavior. Corfidi et al. (1996) and Corfidi (2003) presented a simple and effective method for predicting upwind-propagating MCS motion based on a vertical wind profile from a proximity sounding. These authors separate the MCS motion vector into a contribution by the mean wind through the cloud-bearing layer (advection), and the propensity for individual convective cells to continuously redevelop in the direction of the low-level inflow (propagation), where

$$\mathbf{V}_{\mathrm{MCS}} = \mathbf{V}_{\mathrm{CBL}} - \mathbf{V}_{\mathrm{LLJ}}, \tag{6}$$

$$\mathbf{V}_{\mathrm{CBL}} = \frac{1}{4}(\mathbf{V}_{850} + \mathbf{V}_{700} + \mathbf{V}_{500} + \mathbf{V}_{300}), \quad \text{and} \tag{7}$$

$$\mathbf{V}_{\mathrm{LLJ}} = \mathbf{V}_{850}. \tag{8}$$

Here, the subscript MCS refers to the system motion vector (hereby Corfidi motion vectors, CMVs), CBL refers to the mean wind through the cloud-bearing layer, LLJ refers to the wind velocity of the low-level jet (estimated as the 850-hPa wind velocity in this case), and numeric subscripts indicate wind velocities on isobaric levels.

In section 6 we discussed the propensity for warm-season-type events to exhibit geographically fixed backbuilding, while many of the synoptic-type events simply translated in a line-parallel fashion without backbuilding. This behavior is partially explained by the horizontal distribution of CMVs near the event location. In the case of synoptic-type events, CMVs ranged from ~7 to 10 m s$^{-1}$ near the event location, and tended to be oriented perpendicular (parallel) to the low-level temperature gradient (front) (Fig. 20). In the case of warm-season-type events, however, CMV magnitudes near the event location were smaller and did not parallel the

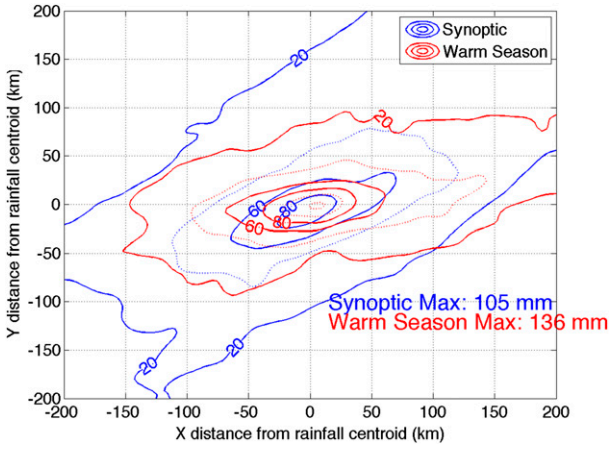


FIG. 18. Composites of 12-h accumulated precipitation (mm) from stage IV precipitation for synoptic-type (dotted blue contours) and warm-season-type (dotted red contours) events (contour intervals are 20 mm). The 12-h precipitation accumulation time frame was temporally centered at the hour of maximum 1-h precipitation accumulation, and spatially centered at the maximum point value within the 1-h period of maximum precipitation accumulation. The 20-, 60-, and 80-mm contours are set in boldface and labeled for the purpose of comparison between the two event types. Maximum precipitation accumulation values are the maximum point value for each event type.

low-level front between 0 and +6 h. Time series of CMV magnitudes at the event locations for both event types, along with the angle between the CMV and a vector perpendicular to the temperature gradient vector (i.e., parallel to the low-level frontal boundary), are shown in Fig. 21. Note that warm-season CMV magnitudes were roughly half those of the synoptic cases, and warm-season vector orientations strayed considerably (>20°) from the low-level frontal orientation, while synoptic CMVs remained nearly perfectly parallel to the low-level front. This analysis provides further evidence that in the case of warm-season-type events, quasi-stationary behavior predominantly resulted from upstream propagation that nearly canceled advection by the mean flow, while in the case of synoptic-type events training predominantly resulted from system motion that paralleled a frontal boundary (and subsequently the linear convective region, which also tended to parallel the frontal boundary).

Our application of the Corfidi vector approach here to estimate MCS motion, though effective at demonstrating key differences in the vertical wind profile characteristics between the two subtypes, may be ultimately insufficient at explaining backbuilding and training due to the mentioned influences of synoptic-scale forcing for ascent on the convective systems that we have considered in this paper, along with their elevated nature [these caveats to the approach are discussed by Corfidi (2003)]. Specifically, while the approach outlined by these authors is shown to be statistically successful at predicting MCS motion, little insight is given into the dynamics that specifically contribute to upwind propagation. For instance, the nose region of the low-level jet provides robust low-level mesoscale lift and is a potential contributor to continuous convective redevelopment (e.g., Stensrud and Fritsch 1993)—especially as it is enhanced nocturnally (which may explain why many of the systems analyzed here exhibited nocturnal peaks in intensity). Furthermore, the convective-scale nonhydrostatic pressure perturbation field immediately adjacent to the convective system may exhibit a low-level nonhydrostatic high pressure maxima (Rotunno and Klemp 1982), given the vertical wind shear profile commonly associated with these systems (Schumacher and Johnson 2005), which would promote continuous convective redevelopment along the southwestern periphery of the system. Additionally, the composite CMV magnitudes discussed in section 5 for warm-season-type events, though smaller than synoptic CMV magnitudes, are nonzero; however, many of the observed warm-season systems remain absolutely stationary for several hours. This further suggests that there are dynamics contributing to upwind propagation in the MCS cases considered in this paper that are not comprehensively explained by the statistical relationship established in the Corfidi studies. A suite of real-data and quasi-idealized numerical simulations of the convective systems considered in this paper have been conducted and are currently being analyzed; through these simulations, and among other goals, we seek to address the mesoscale dynamics that contribute to the upwind propagation of the convective systems analyzed here.

## 6. Summary and discussion

In this study, rotated principal component analysis was applied to the atmospheric fields associated with a large sample of heavy-rain-producing TL/AS MCSs. Cluster analysis in the subspace defined by the leading two resulting RPCs revealed two-distinct synoptic subtypes within the broader TL/AS category, which were referred to as warm-season-type and synoptic-type events, respectively. Separate composites of both types of events revealed synoptic features that have been typically associated with elevated MCSs, such as a southerly low-level jet and meridionally oriented low-level potential temperature gradient to the south, as well as locally maximized isentropic upglide within the region where the MCS initiated and evolved.

Other aspects of the synoptic environments evident in the composite atmospheric fields exhibited considerable differences between the two event types. Warm-season-type

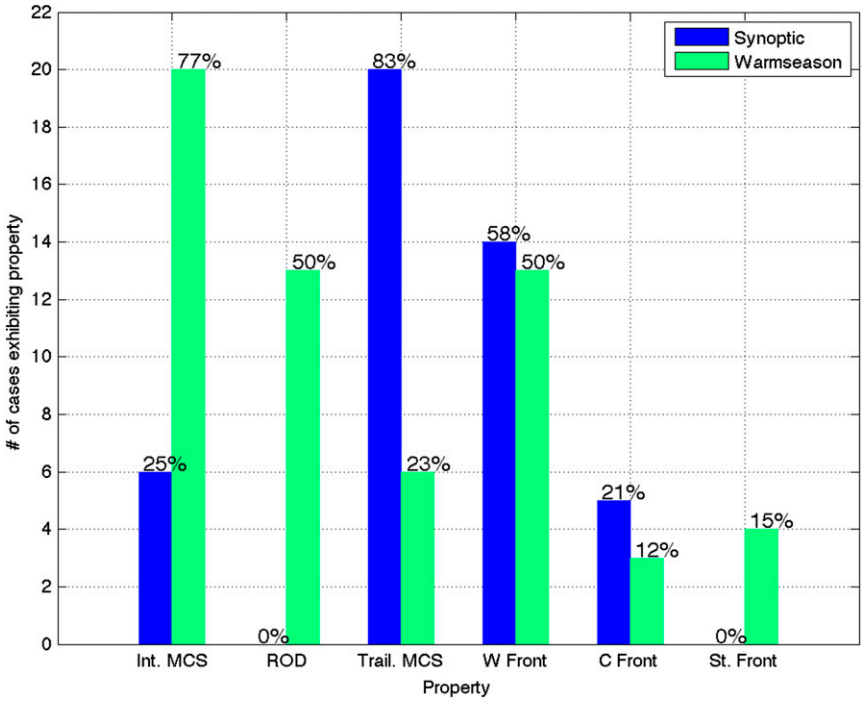


FIG. 19. Summary of frequency of subjectively defined composite radar-reflectivity attributes for each subtype: initial MCS passage prior to TL/AS system (int. MCS), ROD, trailing separate MCS passage at the end of the heavy-rain-producing MCS lifetime (trail. MCS), and heavy-rain-producing MCS occurring on a warm front (W front), cold front (C front), or stationary front (st. front). Bars indicate the numbers of events exhibiting each attribute, and percentage values indicate the percentages of cases within each subtype exhibiting a particular attribute. Note that 23% of warm-season events and 21% of synoptic events did not occur in conjunction with a discernable frontal boundary.

events typically occurred within the right entrance region of a minimally to anticyclonically curved upper-level jet streak, with the warmest low-level air to the southwest. These upper-level thermodynamic and flow regimes are characteristic of the North American summer (hence the name "warm season" given to this event type). On the other hand, synoptic-type events, which tended to exhibit greater horizontal extent than warm-season-type events, typically occurred downstream of a progressive upper-level trough, along a low-level potential temperature gradient with the warmest air to the southeast. These upper-level thermodynamic and flow regimes are more characteristic of the spring and fall transition months, where strong synoptic systems are more prevalent (hence the name "synoptic" given to these events). Synoptic-scale forcing for ascent was typically stronger for synoptic-type events, while low-level moisture was typically greater for warm-season-type events.

Subjectively identified radar reflectivity characteristics and the synoptic frontal boundary type (if any) that the MCS developed along were cataloged for each event type. Synoptic-type events were often followed by the passage of a progressive TS-type MCS, while warm-season-type events were often preceded by the passage of such systems. Roughly 50% of all cases occurred along a nearly stationary warm front, while a few cases occurred near a cold front or did not coincide with a well-defined synoptic boundary. Fifty percent of warm-season-type events exhibited a behavior known as rearward off-boundary development (ROD), whereby linear convection regenerated to the rear of a progressive TS-type MCS, north of the southern periphery of the cold pool generated by the initial system.

Our results from the RPCA applied to atmospheric fields associated with MCS events highlight the utility of such methods as an objective supplement to the current subjective MCS archetype classification methods. Several aspects of the RPCA outcome (and the composites generated therein) are noteworthy within the context of past studies of the types of convective systems considered here—specifically the Maddox et al. (1979) and Schumacher and Johnson (2005) studies, where different types of events are subjectively differentiated from one another.

For instance, some events that clearly constituted a TL/AS radar morphology (e.g., the 23 September 2004

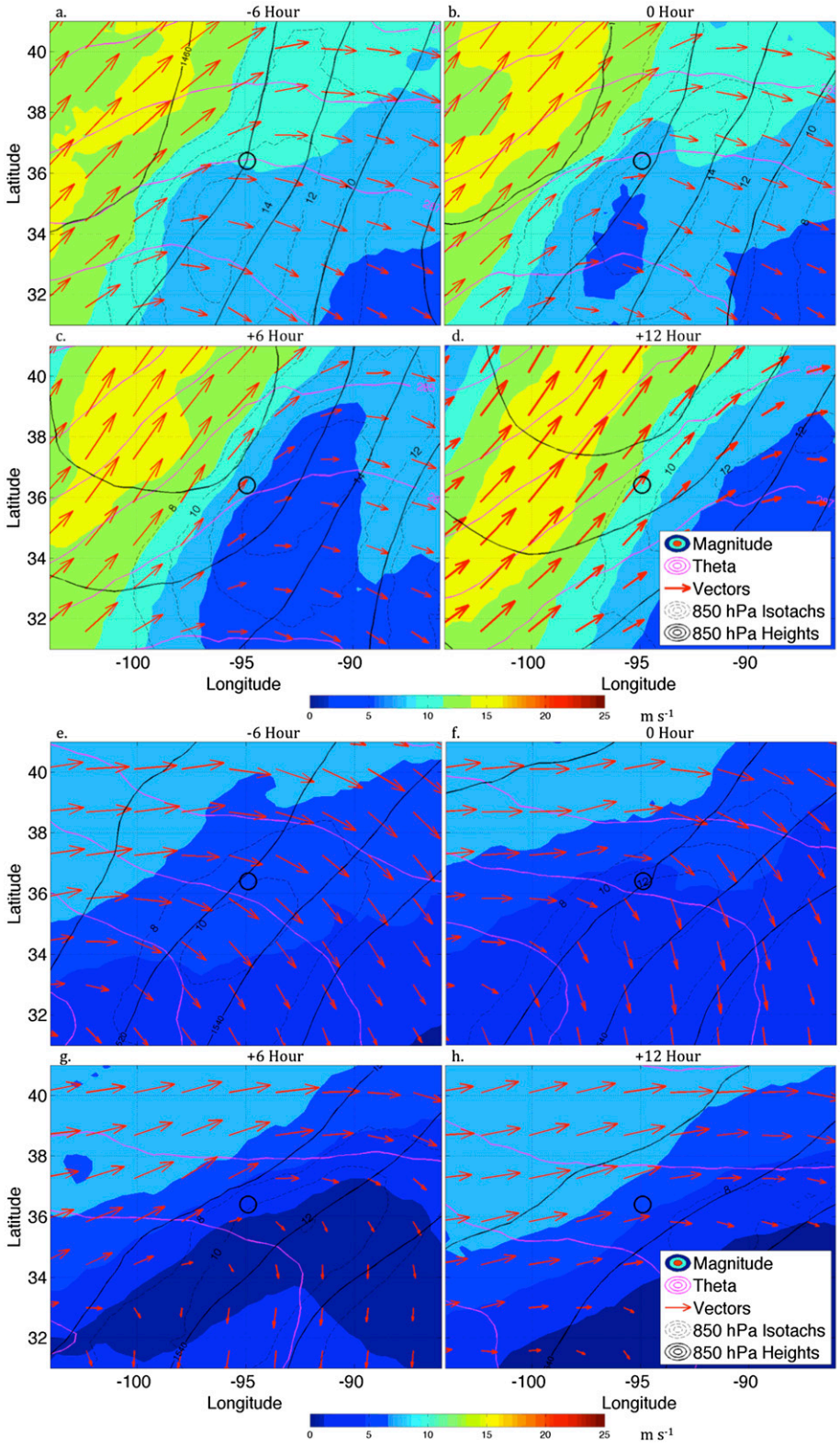


FIG. 20. CMV magnitudes ($m\,s^{-1}$, shading) and vectors (arrows), potential temperature (K, magenta contours), 850-hPa isotachs ($m\,s^{-1}$, dotted contours), and 850-hPa heights (solid black contours at intervals of 20 m; contour locations and values are identical to those in Figs. 7 and 8) for (a)–(d) synoptic-type events and (e)–(h) warm-season-type events.

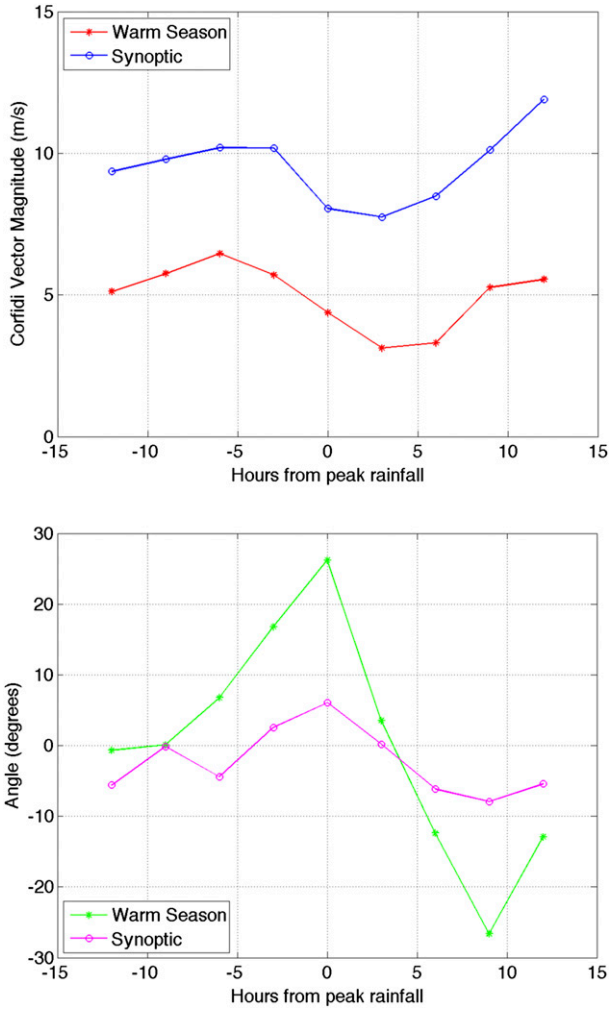


FIG. 21. (top) Time series of CMV magnitudes at the location of peak 1-h rainfall within both the synoptic and warm-season composites. (bottom) Time series of the angle between a unit vector parallel to the CMV, and a unit vector perpendicular to the temperature gradient vector. Times indicate hours from the time where peak 1-h rainfall accumulation occurred at the event location (i.e., −10 h indicates 10 h before peak 1-h rainfall and +10 h indicates 10 h after peak 1-h rainfall).

Ohio River valley and 15 September 2004 Iowa–Minnesota events shown in Fig. 15, which were classified here as synoptic subtype events) occurred within similar synoptic environments to events that would likely be subjectively classified by Maddox et al. (1979) as "synoptic-type events" (e.g., the 2 November 2004 Gulf Coast event). Likewise, other events that also clearly constituted a TL/AS radar morphology (e.g., the 25 May 2005 Kansas and 28 July 2011 Iowa events shown in Fig. 15, which were classified here as warm-season-subtype events) occurred in synoptic environments that were notably different from our synoptic-subtype category; in fact, the composites for the warm-season-type cases subjectively exhibit closer similarities to those from Keene and Schumacher (2013) for bow-and-arrow-type events, and Schumacher and Johnson (2005) for backbuilding/quasi-stationary-type events. The former comparison (to bow-and-arrow events) is supported by the visual similarity of the ROD behavior that is frequently observed here in warm season cases to the bow-and-arrow phenomena, and the latter comparison is supported by the fact that backbuilding behavior was observed in a number of our warm-season-type cases. The overarching observation here is that the dividing lines between case types laid out by the quasi-objective RPCA method do not necessarily coincide with the subjective case classifications based on radar imagery.

From a predictive standpoint, it is noteworthy that two different types of synoptic environments are conducive to heavy-rain-producing convective systems. For instance, a forecaster may notice a short-to-medium-range synoptic-scale environment within a numerical weather prediction model solution that resembles the archetype for synoptic events presented in this study, and make note of the potential for a heavy rain episode in their forecast discussion. During the summer months, however, a forecaster should shift the focus of their analysis of model solutions to recognize synoptic-scale environments that are conducive to warm season events (which, again, exhibit quite different synoptic-scale characteristics).

On a final note, while the analysis presented here has reinforced the salient characteristics commonly associated with quasi-stationary MCSs by previous authors, as well as identified key ways in which these characteristics vary among cases, a valuable supplemental study would involve the comparison between the characteristics of quasi-stationary MCSs and their progressive counterparts (which have not been addressed in any detail here). For instance, while a southwesterly wind direction within the low-level jet (which, by means of propagation, largely cancels the predominantly southwesterly advective component of storm motion as evident in the Corifidi vector analysis) is clearly a salient characteristic of both event types, it is unclear whether this characteristic specifically differentiates slow-moving MCS events from faster-moving progressive MCS events.

A series of real-data and idealized simulations of the MCS archetypes analyzed in this study have been conducted with the aim of better understanding the convective-scale dynamics responsible for heavy rainfall production. These results will be more comprehensively discussed in future articles in order to comprehensively address the convective-scale dynamics associated with TL/AS MCSs, with a specific focus on (among other things) mechanisms for upwind propagation.

*Acknowledgments.* This research was supported by National Science Foundation Grant AGS-1157425. Stage IV precipitation data were obtained from the UCAR Earth Observing Laboratory. NARR data were obtained from the National Climatic Data Center (NCDC) National Operational Model Archive and Distribution system (NOMADS) server. We thank Paul Roebber, George Bryan, Elizabeth Thompson, and anonymous peer reviewers for helpful comments and discussion.

## REFERENCES

Augustine, J. A., and F. Caracena, 1994: Lower-tropospheric precursors to nocturnal MCS development over the central United States. *Wea. Forecasting,* **9,** 116–135, doi:10.1175/1520-0434(1994)009<0116:LTPTNM>2.0.CO;2.

Corfidi, S. F., 2003: Cold pools and MCS propagation: Forecasting the motion of downwind-developing MCSs. *Wea. Forecasting,* **18,** 997–1017, doi:10.1175/1520-0434(2003)018<0997:CPAMPF>2.0.CO;2.

——, J. H. Merritt, and J. M. Fritsch, 1996: Predicting the movement of mesoscale convective complexes. *Wea. Forecasting,* **11,** 41–46, doi:10.1175/1520-0434(1996)011<0041:PTMOMC>2.0.CO;2.

Galarneau, T. J., Jr., L. Bosart, and R. S. Schumacher, 2010: Predecessor events ahead of tropical cyclones. *Mon. Wea. Rev.,* **138,** 3272–3297, doi:10.1175/2010MWR3243.1.

Houze, R. A., Jr., M. I. Biggerstaff, S. A. Rutledge, and B. F. Smull, 1989: Interpretation of Doppler weather radar displays of midlatitude mesoscale convective systems. *Bull. Amer. Meteor. Soc.,* **70,** 608–619, doi:10.1175/1520-0477(1989)070<0608:IODWRD>2.0.CO;2.

——, B. F. Smull, and P. Dodge, 1990: Mesoscale organization of springtime rainstorms in Oklahoma. *Mon. Wea. Rev.,* **118,** 613–654, doi:10.1175/1520-0493(1990)118<0613:MOOSRI>2.0.CO;2.

Jones, T. A., K. M. McGrath, and J. T. Snow, 2004: Association between NSSL mesocyclone detection algorithm-detected vortices and tornadoes. *Wea. Forecasting,* **19,** 872–890, doi:10.1175/1520-0434(2004)019<0872:ABNMDA>2.0.CO;2.

Junker, N. W., R. S. Schneider, and S. L. Fauver, 1999: A study of heavy rainfall events during the Great Midwest Flood of 1993. *Wea. Forecasting,* **14,** 701–712, doi:10.1175/1520-0434(1999)014<0701:ASOHRE>2.0.CO;2.

Keene, K. M., and R. S. Schumacher, 2013: The bow and arrow mesoscale convective structure. *Mon. Wea. Rev.,* **141,** 1648–1672, doi:10.1175/MWR-D-12-00172.1.

Laing, A. G., and J. M. Fritsch, 2000: The large-scale environments of the global populations of mesoscale convective complexes. *Mon. Wea. Rev.,* **128,** 2756–2776, doi:10.1175/1520-0493(2000)128<2756:TLSEOT>2.0.CO;2.

Lin, Y., and K. E. Mitchell, 2005: The NCEP stage II/IV hourly precipitation analyses: Development and applications. Preprints, *19th Conf. on Hydrology,* San Diego, CA, Amer. Meteor. Soc., 1.2. [Available online at https://ams.confex.com/ams/pdfpapers/83847.pdf.]

Maddox, R. A., 1980: Mesoscale convective complexes. *Bull. Amer. Meteor. Soc.,* **61,** 1374–1387, doi:10.1175/1520-0477(1980)061<1374:MCC>2.0.CO;2.

——, 1983: Large-scale meteorological conditions associated with midlatitude, mesoscale convective complexes. *Mon. Wea. Rev.,* **111,** 1475–1493, doi:10.1175/1520-0493(1983)111<1475:LSMCAW>2.0.CO;2.

——, C. F. Chappell, and L. R. Hoxit, 1979: Synoptic and meso-α-scale aspects of flash flood events. *Bull. Amer. Meteor. Soc.,* **60,** 115–123, doi:10.1175/1520-0477-60.2.115.

Mercer, A. E., C. M. Shafer, C. A. Doswell, L. M. Leslie, and M. B. Richman, 2012: Synoptic composites of tornadic and non-tornadic outbreaks. *Mon. Wea. Rev.,* **140,** 2590–2608, doi:10.1175/MWR-D-12-00029.1.

Mesinger, F., and Coauthors, 2006: North American Regional Reanalysis. *Bull. Amer. Meteor. Soc.,* **87,** 343–360, doi:10.1175/BAMS-87-3-343.

Monaghan, A. J., D. L. Rife, J. O. Pinto, C. A. Davis, and J. R. Hannan, 2010: Global precipitation extremes associated with diurnally varying low-level jets. *J. Climate,* **23,** 5065–5084, doi:10.1175/2010JCLI3515.1.

Moore, J. T., F. H. Glass, C. E. Graves, S. M. Rochette, and M. J. Singer, 2003: The environment of warm-season elevated thunderstorms associated with heavy rainfall over the central United States. *Wea. Forecasting,* **18,** 861–878, doi:10.1175/1520-0434(2003)018<0861:TEOWET>2.0.CO;2.

Parker, M. D., and R. H. Johnson, 2000: Organizational modes of midlatitude mesoscale convective systems. *Mon. Wea. Rev.,* **128,** 3413–3436, doi:10.1175/1520-0493(2001)129<3413:OMOMMC>2.0.CO;2.

Pitchford, K. L., and J. London, 1962: The low-level jet as related to nocturnal thunderstorms over Midwest United States. *J. Appl. Meteor.,* **1,** 43–47, doi:10.1175/1520-0450(1962)001<0043:TLLJAR>2.0.CO;2.

Richman, M. B., 1986: Rotation of principal components. *J. Climatol.,* **6,** 293–335, doi:10.1002/joc.3370060305.

Rotunno, R., and J. B. Klemp, 1982: The influence of the shear-induced pressure gradient on thunderstorm motion. *Mon. Wea. Rev.,* **110,** 136–151, doi:10.1175/1520-0493(1982)110<0136:TIOTSI>2.0.CO;2.

Schaefer, J., and C. A. Doswell III, 1984: Empirical orthogonal function expansion applied to progressive tornado outbreaks. *J. Meteor. Soc. Japan,* **62,** 929–936.

Schumacher, R. S., 2009: Mechanisms for quasi-stationary behavior in simulated heavy-rain-producing convective systems. *J. Atmos. Sci.,* **66,** 1543–1568, doi:10.1175/2008JAS2856.1.

——, and R. H. Johnson, 2005: Organization and environmental properties of extreme-rain-producing mesoscale convective systems. *Mon. Wea. Rev.,* **133,** 961–976, doi:10.1175/MWR2899.1.

——, and ——, 2006: Characteristics of U.S. extreme rain events during 1999–2003. *Wea. Forecasting,* **21,** 69–85, doi:10.1175/WAF900.1.

——, and ——, 2008: Mesoscale processes contributing to extreme rainfall in a midlatitude warm-season flash flood. *Mon. Wea. Rev.,* **136,** 3964–3986, doi:10.1175/2008MWR2471.1.

Stensrud, D. J., and J. M. Fritsch, 1993: Mesoscale convective systems in weakly forced large-scale environments. Part I: Observations. *Mon. Wea. Rev.,* **121,** 3326–3344, doi:10.1175/1520-0493(1993)121<3326:MCSIWF>2.0.CO;2.

Thompson, D. W. J., and J. M. Wallace, 1998: The Arctic Oscillation signature in the wintertime geopotential height and temperature fields. *Geophys. Res. Lett.,* **25,** 1297–1300, doi:10.1029/98GL00950.

Tuttle, J. D., and C. A. Davis, 2006: Corridors of warm season precipitation in the central United States. *Mon. Wea. Rev.,* **134,** 2297–2317, doi:10.1175/MWR3188.1.

Wilks, D. S., 2006: *Statistical Methods in the Atmospheric Sciences.* Academic Press, 627 pp.